A Level Set Method for an Inverse Problem Arising in Photolithography

A DISSERTATION
SUBMITTED TO THE FACULTY OF THE GRADUATE SCHOOL
OF THE UNIVERSITY OF MINNESOTA
BY

Vasfiye Hande Tüzel

IN PARTIAL FULFILLMENT OF THE REQUIREMENTS
FOR THE DEGREE OF
DOCTOR OF PHILOSOPHY

Fadil Santosa

July, 2009

Acknowledgements

I am deeply indebted to my advisor Dr. Fadil Santosa. His enthusiasm for science and integral view on research and his mission for providing only high-quality work and not less, has inspired me and enriched my growth as a scientist. I owe him lots of gratitude for his supervision, advice, and guidance at every stage of my graduate career. I am also most grateful to Director of Graduate Studies Dr. Richard McGehee for his tremendous support.

Finally, I am greatly indebted to my dear husband, my closest friend, Erkan, who always put my interests before his. His love, support without any complaints, and his constant encouragement has enabled me to complete this work.

Dedication

This dissertation is dedicated to my dear husband Erkan Tüzel.

Table of Contents

List of Figures

List of Abbreviations

IC	:	Integrated Circuit
MEMS	:	Micro-electro-mechanical Systems
RETs	:	Resolution Enhancement Techniques
TCC	:	Transmission Cross Coefficients
SOCS	:	Sum of Coherent Systems
OCA	:	Optimal Coherent Approximation
SVD	:	Singular Value Decomposition
HWHM	:	Half Width at Half Maximum
PDE	:	Partial Differential Equations
CFL	:	Courant-Friedrichs-Levy
FMM	:	Fast Marching Method

Chapter 1

Introduction

Integrated circuits (ICs) and other micro-electro-mechanical systems (MEMS) devices have become integral components of technological tools we use in everyday life. There is a growing demand for developing smaller and smaller circuit components, or designing nano-fabricated devices that have many applications ranging from medicine to defense. However, as these circuit components become smaller, problems arise in the manufacturing these elements, and one of the limitations at these small scales is achieving accuracy.

A typical process used in production of ICs, also known as microchips, is *optical lithography*. It is a process of transferring layout patterns to a substrate using a mask, under an ultraviolet light source—very similar to photoprinting. We describe this process in more detail in Section 1.1. Even though this is a very successful technique, for a long time it has been predicted that the process would be limited in success due to finite wavelength of the light used to project circuit images—the wavelength would be too large to resolve the fine details demanded by the ever shrinking microchip designs.

However, both the semiconductor and nano-fabrication industry kept optical lithography alive using several strategies such as i) decreasing the wavelength of light, ii) improving the optical equipments, and iii) using the so-called *resolution enhancement techniques* (RETs) to resolve finer details in designs by manipulating masks. We give a brief introduction to these approaches in Section 1.2. The RETs provide one of the most promising approaches, and in the past decade there has been interest in formulating the

problem of designing enhanced masks as an inverse problem. The reader is introduced to the field of *inverse lithography* in Section 1.3, where we also discuss our approach to this inverse problem and give a brief outline of the thesis.

1.1 Photolithography Process

As mentioned earlier, photolithography is a key process used in semiconductor fabrication to create the integrated circuits [4]. The process is very similar to photoprinting, in which the patterns that will become layers of an integrated circuit are exposed on a semiconductor wafer, one layer at a time (see Figure 1.1).

The first step in the process is the preparation of the substrate—a silicon wafer—typically coated with layers of silicon nitride and silicon dioxide, followed by a photo sensitive polymer, called the *photoresist* (see Part 1 of Figure 1.1). These materials are soluble when they interact with light, therefore upon exposing them to UV light and developing, the surface can be rinsed off the polymer. One can, therefore, imprint a particular design on the wafer by blocking light exposure to certain areas of the substrate. This is done by using a *mask* between the projector and the substrate as depicted in Part 2 of Figure 1.1. Such a mask is typically designed on the computer and printed on a quartz plate by depositing chrome [1, 4]. The pattern creates dark and light regions that correspond to physical elements of the IC—typically parts of transistors or connections between them—to be reproduced on each chip location on the wafer [4]. It is important to note that photoresists have threshold values beyond which they react to light and become soluble, therefore the intensity of the light that is projected onto the substrate also plays a crucial role [5].

Once the imprinting using the mask is complete, the wafer will have areas that are protected by the photoresist together with exposed silicon dioxide. In the next step, regions that are not protected by the phoresist are removed by a process called *etching*. The duration of etching will determine the depth of the removed areas, and with additional deposition of dielectric materials and metals, or ion implantation, the desired electrical characteristics will be formed on the silicon [4]. This process is continued until

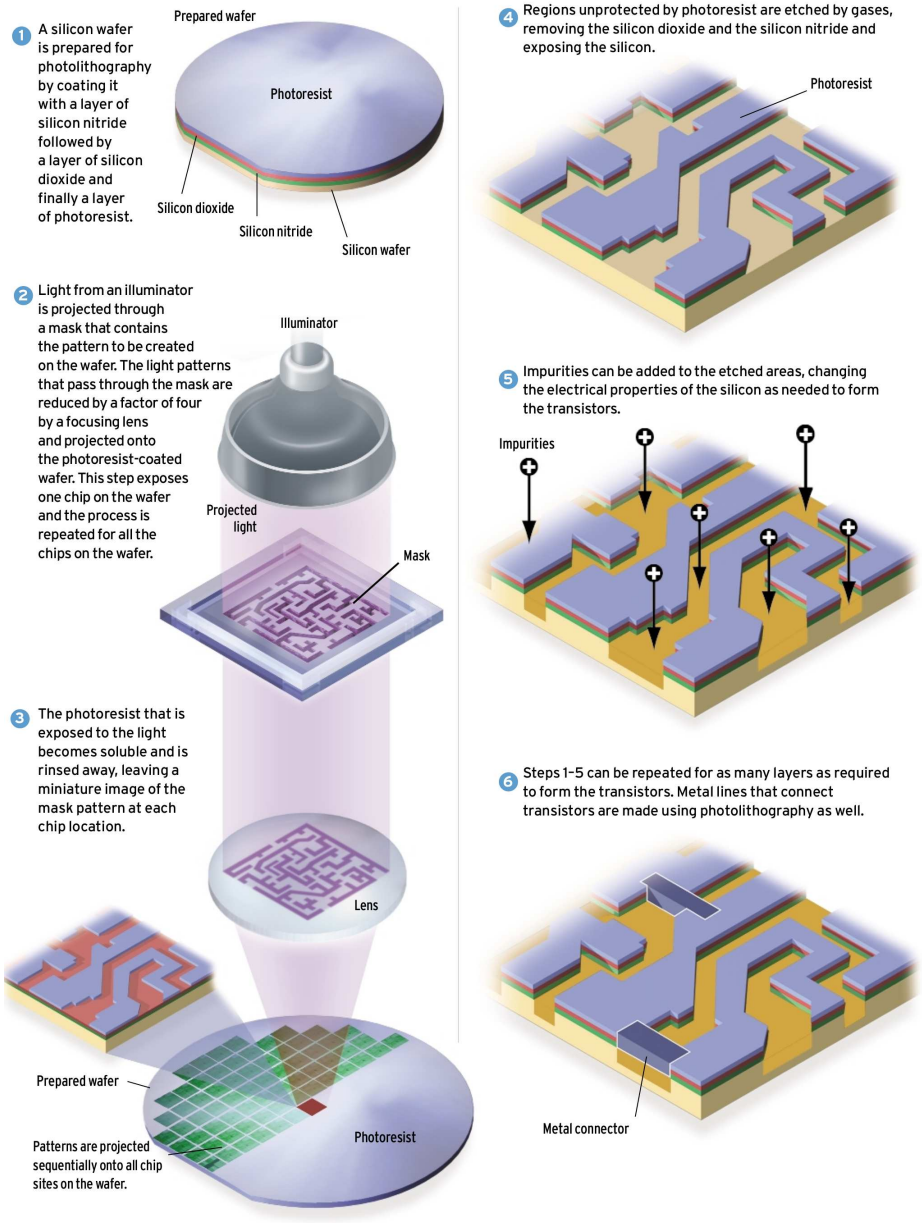

Figure 1.1: Optical lithography, similar to photographic printing, creates patterns in a layer of photoresist that coats a prepared silicon wafer. Once the patterns are created, the elements of the integrated circuit are formed by etching, depositing material or ion implantation (from [1]).

all the transistors and wires are assembled, layer by layer. As many as 30 masks are used to produce the various layers of a typical IC.

One important component in this process is obviously the projector. Typically, very high quality projectors and sophisticated lens and mirror systems are used to make sure that the projected light has the desired coherence and intensity. A large lens collects the transmitted light through the mask and focuses it on the wafer to create a scaled-down image. As a result, patterns are projected sequentially onto all sites on the wafer as as shown in Part 3 of Figure 1.1. The sine of the largest angle incident on the wafer is called the numerical aperture (NA) of the lens. The aperture is similar to the f-stop in photography, in that a larger aperture allows higher resolution but reduces the depth of focus—like the depth of field in photography [1].

Even though lithography is a powerful technique, widely used by the semiconductor industry, it has several limitations if one wants to manufacture ICs with nanometer resolution. Several problems arise from the small dimensions of the features, the finite size, and inherent limitations of the imaging system. First, the high frequency components required to reproduce the sharp edges in mask features may fall outside the lens. In addition, incident light passing through two locations on the mask within close proximity interact and the final shapes may have rounded corners or may even bulge towards adjacent shapes—possibly connecting wrong spots and rendering the chip defective in worst case scenarios. In the next section, we discuss these limitations and possible solutions.

1.2 Improvements in Photolithography Process

The limits of optical imaging were first described over a century ago by Ernst Abbe [1]. He showed that the narrow features in such as lines and spaces in patterns projected by an optical system are directly proportional to the wavelength of the light used, and inversely proportional to the numerical aperture, NA. Hence, the smaller the wavelength and larger the NA of the lens, better the resolution. To overcome these limitations, semiconductor industry continuously decreased the wavelength from 365 nm in the

1980s down to 193 nm in the most advanced systems today using argon-fluoride lasers. These systems are producing ICs with hundreds of millions of transistors with smallest features of the order of 100 nm. There are also some recent efforts using a laser with fluorine alone to reduce the wavelength to 157 nm to be able to design ICs with features of 65 nm or smaller [6].

To increase the numerical aperture for better resolution, lens designers have been creating lenses with larger diameters and more lens elements to collect more of the light emerging from the mask. When introduced in the 70s, the first reduction-system lenses had a numerical aperture of 0.2 [1], and nowadays a value of 0.63 is quite common. The newest lithography systems have been announced to have apertures of 0.85 [1]. A numerical aperture at the theoretical maximum of 1 is possible only with an infinitely large lens, collecting 100% of the light from the mask. In addition to the numerical aperture, there are many other factors that affect image quality. Lenses do not always form perfect images, and there is always some degree of distortion, also known as *aberration* caused by the lens. By careful design of the lenses manufacturers try to minimize these aberrations.

Besides improving lenses and lasers, IC manufacturers also use the so-called resolution enhancement techniques (RETs), and in one way or another, they all coax the light into resolving shapes much smaller than its wavelength. The main techniques are Optical Proximity Correction (OPC), phase shifting masks, and modified, "off axis" illumination [1]. Since the progress in developing better lasers and optical setups is relatively slower, RETs are absolutely critical to the future progress of the rapidly developing semiconductor technology.

Optical Proximity Correction is one of the widely used enhancement techniques in the mask design process. OPC is the process of modifying the masks that are drawn by the designers to compensate for the non-ideal properties of the lithography process. The process is illustrated in Figure 1.2. For instance, the approach proposed by Cobb and Zakhor [7] for OPC mask design consists of parametrizing the mask using polygons, and fragmenting the mast pattern into edges and corners. These elements are then modified, moved around or additional small features are added to the mask until the

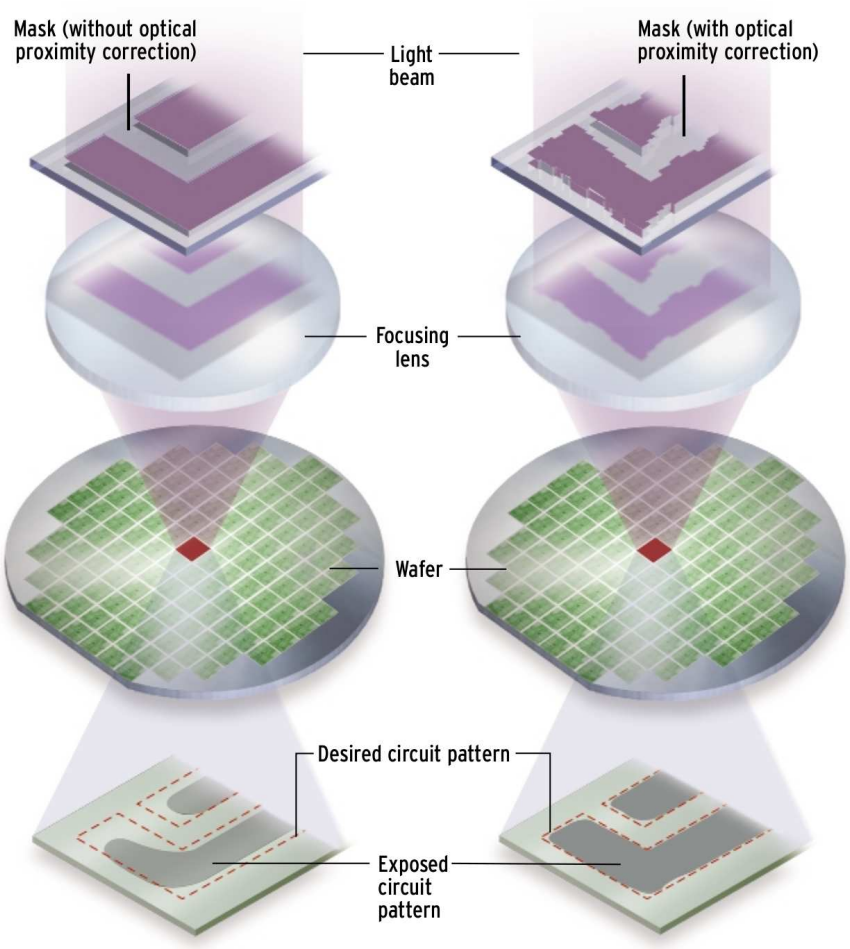

Figure 1.2: Illustration of the optical proximity correction (OPC) approach. Taken from Ref. [1].

final pattern on the substrate is satisfactory [8]. These modifications done at strategic locations on the mask significantly improve the yield and process reliability. Figure 1.3 shows the effectiveness of the OPC approach for a sample mask [2]. After the correction the resulting intensity is very close to the pattern of the ideal mask.

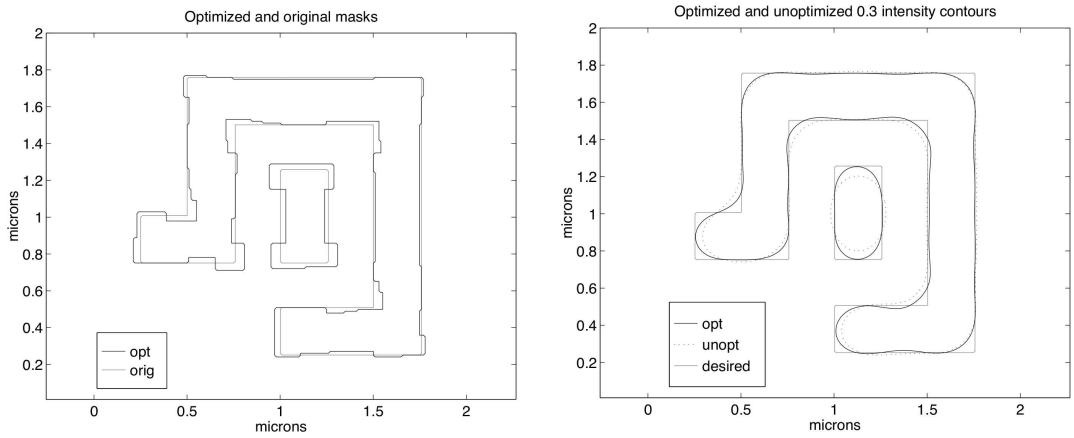

(a) (b)

Figure 1.3: The results of applying OPC to a simple mask layout to reduce corner rounding. (a) Overlayed original and optimized masks (b) overlayed original and optimized intensities (taken from [2]).

1.3 Lithography as an inverse problem

While the OPC approaches mentioned above improve lithography, they have a number of shortcomings. The approach is primarily local, i.e. the changes are done locally on the edges and corners [8], and therefore the process can not be automated, and extra verification steps are necessary [8]. Since trying to find the optimum mask design by trial and error is an inefficient approach, there has been interest in formulating this as an inverse problem, the so-called *inverse lithography*. Inverse lithography is an image design problem which consists of finding an image that when used as an input to the given imaging system results in the desired output image within error. In other words, given a desired geometric pattern on the silicon wafer, we want to find a mask design such that the final pattern remaining after a complete lithography process is as close as possible to the desired pattern.

One of the earlier works on this inverse problem was done by Sayegh et al. [9] where

they have used a linear-programming technique to do OPC. Later iterative alternating projections [10] and mixed linear programming techniques [11] were employed to improve accuracy. Pati and Kaliath [12] introduced a decomposition of partially coherent systems—the so-called Optimal Coherent Approximation (OCA)—as the sum of coherent imaging systems (by using Mercer expansion) to design phase shift masks. Liu and Zakhor [13] formulated the problem as the minimization of the L_2 norm between the ideal and the actual wafer images, and used simulated annealing to synthesize binary and phase shift masks. Improving on this approach, Peckerar and co-workers used gradient based optimization techniques to minimize the cost function [14, 15, 16]. The reader is referred to the work by Granik [17] for a review of linear programming based approaches. More recently Poonawala and Milanfar proposed a new framework and used a gradient descent algorithm to design the optimum binary image masks, and generalized their approach to coherent, incoherent and partially coherent systems [8].

We follow a similar path in this thesis, and describe the lithography process as an inverse problem. In Chapter 2, we review the fundamentals of scalar diffraction theory and introduce our notation. The forward problem is described in Chapter 3, where we calculate the aerial image intensity on the substrate, given the properties of the system and a mask. This is done using scalar diffraction theory, and the Helmholtz equation under the Kirchoff approximation. We also employ the sum of coherent systems approach (SOCS) described by Cobbs [2]. The SOCS structure is most similar to OCA described in Ref. [12]. Once the forward problem is solved, we then formulate the inverse problem, define a cost function and minimize it in a least square sense as described in Chapter 4. The key difference in our approach is that we use level set methods to solve the inverse problem. By using calculus of variations we show that solving the inverse problem is equivalent of solving a Hamilton-Jacobi equation. In Chapter 4, we also describe our numerical algorithm, give results for different size and design masks, and discuss the convergence. In the final chapter, we provide a summary of the thesis, and an outlook for the future.

Chapter 2

Background in Scalar Diffraction Theory

In this chapter, we discuss scalar diffraction theory for monochromatic waves with a single wavelength. We start with a short introduction to electomagnetic theory in Section 2.1. In Section 2.2, we derive the Helmholtz equation and convert it into the Helmholtz-Kirchhoff Integral equation by using the Green's theorem. We then discuss the application of this integral for diffraction by a plane screen. In Section 2.3, the Kirchhoff boundary conditions are discussed. We then remove the inconsistencies of the Kirchhoff theory by reformulating the problem using Rayleigh-Sommerfeld theory of diffraction in Section 2.4. In Section 2.5, we discuss the angular spectrum of the incident wave and we end the chapter with a summary.

2.1 A Short Introduction to Electromagnetic Theory

James Clerk Maxwell identified light as "an electromagnetic disturbance in the form of waves propagated through the electromagnetic field according to electromagnetic laws" [18]. The electromagnetic state of a point in vacuum is described by the electric, **E**, and magnetic, **H**, fields. Electric fields are generated by electric charges. Magnetic fields are generated by charges in motion, *i.e.* by electric currents. These two fields are coupled and each can be generated (or induced) by time variation of the other. However, **E** and **H** are de-coupled when the two fields do not vary with time. For time dependent

electric and magnetic fields, Maxwell equations are given by

$$\boldsymbol{\nabla} \cdot \mathbf{E} = 0 \,, \tag{2.1}$$

$$\boldsymbol{\nabla} \cdot \mathbf{H} = 0 \,, \tag{2.2}$$

$$\boldsymbol{\nabla} \times \mathbf{E} = -\mu_0 \frac{\partial \mathbf{H}}{\partial t} \,, \tag{2.3}$$

$$\boldsymbol{\nabla} \times \mathbf{H} = -\epsilon_0 \frac{\partial \mathbf{E}}{\partial t} \,. \tag{2.4}$$

Here the constant μ_0 is known as the *permeability* of vacuum and the constant ϵ_0 is called the *permittivity* of the vacuum [19]. By taking the curl of Eqs. (2.3) and (2.4) followed by some algebraic manipulations we find that both fields $\mathbf{E}$ and $\mathbf{H}$ separately satisfy the following partial differential equation known as the wave equation;

$$\nabla^2(\ \ ) = \frac{1}{c^2} \frac{\partial^2(\ \ )}{\partial t^2} \,, \tag{2.5}$$

where $c \equiv (\mu_0 \epsilon_0)^{-1/2}$ is the *speed of light* in vacuum. Here, we have used the following vector identity for an arbitrary field

$$\boldsymbol{\nabla} \times (\boldsymbol{\nabla} \times \mathbf{E}) = \boldsymbol{\nabla} (\boldsymbol{\nabla} \cdot \mathbf{E}) - \nabla^2(\mathbf{E}) \,. \tag{2.6}$$

Equation (2.5) implies that the changes in the fields $\mathbf{E}$ and $\mathbf{H}$ propagate through empty space with a speed of light c. In SI units, c is approximately equal to 3×10^8 m/s.

Since the vector wave equation given by Eq. (2.5) is obeyed by both $\mathbf{E}$ and $\mathbf{H}$, an identical scalar wave equation is obeyed by all components of these vectors. One can therefore summarize the behavior of all components of $\mathbf{E}$ and $\mathbf{H}$, in vacuum, through a single wave equation

$$\nabla^2 u(P,t) = \frac{1}{c^2} \frac{\partial^2 u(P,t)}{\partial t^2} \,, \tag{2.7}$$

where $u(P,t)$ represents any of the scalar field components, depending on position P and time t.

2.2 The Helmholtz Equation

Let us now consider a scalar function, $u(P,t)$, representing either an electric or magnetic field component—call it the light disturbance—at position $P = (x, y, z)$ and time t. For a strictly monochromatic scalar wave, the scalar field $u(P,t)$ could be written as

$$u(P,t) = A(P)\cos\left[\omega t - \psi(P)\right] \tag{2.8}$$

where $\omega = 2\pi\nu$ is the *angular frequency* and ν is the *frequency* of the wave. Eq. (2.8) can be also expressed in the form

$$u(P,t) = \mathrm{Re}\left\{\, U(P)\, e^{-i\omega t} \,\right\}, \tag{2.9}$$

where the complex function $U(P)$, known as the *complex amplitude* or *phasor* of the disturbance given by

$$U(P) = A(P)\, e^{i\psi(P)}\,.$$

Here $A(P)$ and $\psi(P)$ are the real-valued *amplitude* and *phase* of the wave at the position P, respectively.

Since $u(P,t)$ represents an optical wave, it must satisfy the scalar wave equation given by Eq. (2.7) at each source-free point. Substituting Eq. (2.9) into Eq. (2.7) yields the following time-independent wave equation, known as *the Helmholtz equation*,

$$\left(\nabla^2 + k^2\right) U = 0\,, \tag{2.10}$$

for the complex-valued function U in vacuum. Here $k = \omega/c = 2\pi/\lambda$ is called the *wave number* and λ is the *wavelength*.

2.2.1 Green's Theorem

We now seek a solution to the Helmholtz equation in Eq. (2.10) in the presence of obstacles, *i.e.* a solution that satisfies the boundary conditions imposed by the obstacles. In order to find this solution we first need to implement the use of Green's theorem which

can be stated as follows:

Let $U(P)$ and $G(P)$ be any two, complex-valued, scalar functions of position, and let V be a volume surrounded by a closed surface S. If U, G, and their first and second partial derivatives are continuous within V and on S, then we have

$$\iiint_V \left(G\nabla^2 U - U\nabla^2 G\right) \mathrm{d}v = \iint_S \left(U\frac{\partial G}{\partial n} - G\frac{\partial U}{\partial n}\right) \mathrm{d}s \tag{2.11}$$

where $\partial/\partial n$ represents a directional derivative in the outward unit normal direction at each point on S.

This theorem could be considered to be a primary foundation of the scalar diffraction theory. It is important to note that a good choice of an auxiliary function G and a closed surface S is needed for its direct application to a diffraction problem [20].

2.2.2 The Helmholtz-Kirchhoff Integral Theorem

Let $P_0 = (x_0, y_0, z_0)$ be the observation point surrounded by an arbitrary closed surface S and V be the volume bounded by S. We want to express the optical disturbance at the observation point in terms of the surface integral over S, which in turn can be evaluated by making certain approximations. In order to find this relation we need to apply the Green's theorem. Therefore we choose the function G, for an arbitrary point $P_1 = (x, y, z)$ on an arbitrary closed surface S, to be a three dimensional, free-space Green's function, *i.e.* in the form of a spherically symmetric wave traveling out from the observation point P_0 as the origin. Namely

$$G(P_1) = \frac{e^{ikr_0}}{r_0}, \tag{2.12}$$

where $r_0 = |\mathbf{r_0}| = |\overrightarrow{P_0P_1}| = \sqrt{(x-x_0)^2 + (y-y_0)^2 + (z-z_0)^2}$. Note that k is the magnitude of the wave vector, $\mathbf{k} = k_x\mathbf{e_x} + k_y\mathbf{e_y} + k_z\mathbf{e_z}$, previously defined in Eq. (2.10) . However, since the continuity of the function G and its first and second partial derivatives is required, we apply the Green's theorem to a region of space surrounding, but excluding, the observation point P_0 as shown in Figure 2.1 [20, 21]. Hence, we split

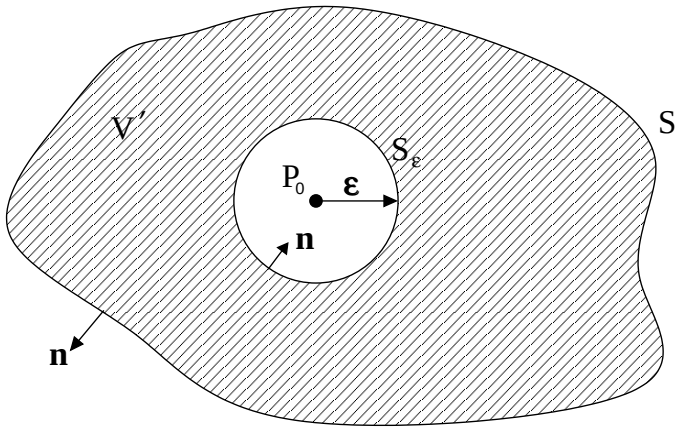

Figure 2.1: Surface of integration for Helmholtz-Kirchhoff Integral Theorem. Here P_0 is the observation point and **n** represents the outward and inward unit normals on the surfaces S and S_ϵ, respectively.

the surface integral into two portions to exclude the discontinuity at P_0. One over the surface S on which the incident wave disturbance is presumed known, and over a small spherical surface S_ϵ of radius ϵ centered at P_0. Here V' is the volume bounded by these two closed surfaces S and S_ϵ and we choose the Green's function G given in Eq. (2.12) for an arbitrary point $P_1 = (x, y, z)$ on the new surface of integration $S' = S + S_\epsilon$. Within the volume V', the disturbance G then satisfies the Helmholtz equation $\left(\nabla^2 + k^2\right) G = 0$. On the other hand, we assume that the sources that generate the actual wave U are all located outside of the surface S, so that U satisfies the Helmholtz equation (2.10) in the volume V enclosed by the surface S. Therefore by substituting these equations to the left hand side of the Green's formula (2.11) we observe that

$$\iiint_{V'} \left(G\nabla^2 U \, - \, U\nabla^2 G\right) \mathrm{d}v = - \iiint_{V'} \left(GUk^2 \, - \, UGk^2\right) \mathrm{d}v \equiv 0 \, . \tag{2.13}$$

Hence the Green's formula over V' reduces to

$$\iint\limits_{S'=S+S_\epsilon} \left(U\frac{\partial G}{\partial n} - G\frac{\partial U}{\partial n} \right) \mathrm{d}s = 0 \,,$$

or

$$\iint\limits_{S} \left(U\frac{\partial G}{\partial n} - G\frac{\partial U}{\partial n} \right) \mathrm{d}s = -\iint\limits_{S_\epsilon} \left(U\frac{\partial G}{\partial n} - G\frac{\partial U}{\partial n} \right) \mathrm{d}s \,, \tag{2.14}$$

where the unit normal vector $\mathbf{n}$ is outward in the conventional sense on S, but inward, towards P_0 on S_ϵ (see Figure 2.1).

In order to carry out the surface integrals we also need to evaluate the derivative of the Green's function on the surface S'. From Eq. (2.12), for an arbitrary point P_1 on S', we obtain

$$\frac{\partial G(P_1)}{\partial n} = \nabla G \cdot \mathbf{n} = \cos(\mathbf{n}, \mathbf{r_0}) \left(ik - \frac{1}{r_0} \right) \frac{e^{ikr_0}}{r_0} \,, \tag{2.15}$$

where $\cos(\mathbf{n}, \mathbf{r_0})$ is the cosine of the angle between the normal $\mathbf{n}$ and the vector $\mathbf{r_0}$ joining P_0 to P_1. For any point P_1 on the surface S_ϵ, $\cos(\mathbf{n}, \mathbf{r_0}) = \cos(\mathbf{n}, \boldsymbol{\epsilon}) = -1$ and Eqs. (2.12) and (2.15) become

$$G(P_1) = \frac{e^{ik\epsilon}}{\epsilon} \,,$$

and

$$\frac{\partial G(P_1)}{\partial n} = \left(\frac{1}{\epsilon} - ik \right) \frac{e^{ik\epsilon}}{\epsilon} \,.$$

In the limit of arbitrarily small ϵ we obtain

$$\lim_{\epsilon \to 0} \iint\limits_{S_\epsilon} G\frac{\partial U}{\partial n} \mathrm{d}s = \lim_{\epsilon \to 0} 4\pi\epsilon^2 \left(\frac{e^{ik\epsilon}}{\epsilon} \right) \left(\frac{\partial U}{\partial n} \right) = 0 \,,$$

and

$$\lim_{\epsilon \to 0} \iint\limits_{S_\epsilon} U\frac{\partial G}{\partial n} \mathrm{d}s = \lim_{\epsilon \to 0} 4\pi\epsilon^2 \left(\frac{1}{\epsilon} - ik \right) \left(\frac{e^{ik\epsilon}}{\epsilon} \right) U = 4\pi\, U(P_0) \,.$$

Substituting these into Eq. (2.14) and using the fact that U and its derivatives are

continuous at P_0 yields

$$\iint\limits_S \left(U\frac{\partial G}{\partial n} - G\frac{\partial U}{\partial n} \right) \mathrm{d}s = -\lim_{\epsilon \to 0} \iint\limits_{S_\epsilon} \left(U\frac{\partial G}{\partial n} - G\frac{\partial U}{\partial n} \right) = -4\pi\, U(P_0)\ ,$$

or

$$U(P_0) = \frac{1}{4\pi} \iint\limits_S \left(G\frac{\partial U}{\partial n} - U\frac{\partial G}{\partial n} \right) \mathrm{d}s\,. \tag{2.16}$$

This result, known as *the Helmholtz-Kirchhoff integral theorem*, allows the time-harmonic scalar wave U at an observation point P_0 to be expressed in terms of its "boundary values" over any enclosing surface S. We now need to carefully choose our surface of integration and find reasonable approximations to these values on S [20, 21].

2.2.3 Application of the Integral Theorem for the Diffraction by a Plane Screen

Let us now consider the problem of diffraction of light by a planar aperture in an infinite opaque screen, as illustrated in Figure 2.2. In order to use Helmholtz-Kirchhoff theorem, we need to choose a proper surface of integration. We chose the closed surface S to consist of two parts, namely S_P and S_R as shown in Figure 2.2. Here, the plane surface S_P, lying adjacent to the diffracting screen, is joined by a large spherical cap, S_R, which is of radius R and centered at the observation point P_0. The closed surface S is then the sum of S_P and S_R, and Eq. (2.16) becomes

$$U(P_0) = \frac{1}{4\pi} \iint\limits_{S_P+S_R} \left(G\frac{\partial U}{\partial n} - U\frac{\partial G}{\partial n} \right) \mathrm{d}s\,. \tag{2.17}$$

Let us now focus on the surface integral on S_R. At any point P_1 on S_R, the Green's function is given by

$$G(P_1) = \frac{e^{ikR}}{R}\ , \tag{2.18}$$

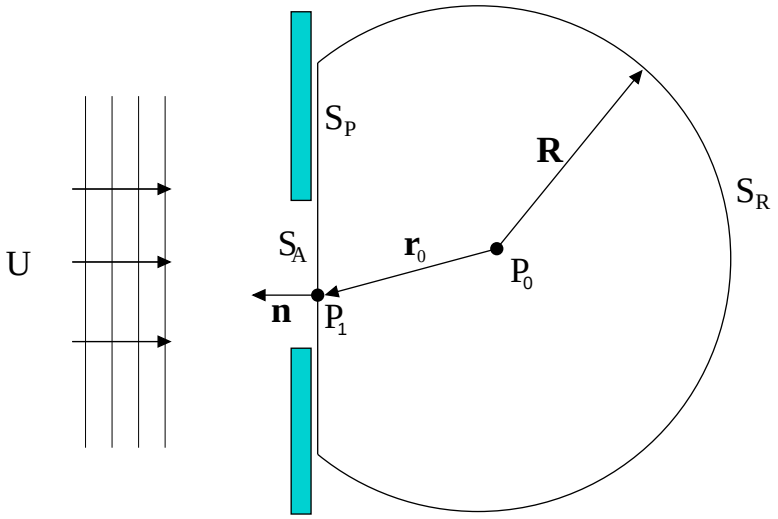

Figure 2.2: Geometry used for Kirchoff formulation for diffraction by a planar apperture. The apperture is illuminated by a known field U from the left. Surface of integration is $S = S_P + S_R$. P_0 is the observation point.

where $R = |\mathbf{R}| = |\overrightarrow{P_0P_1}|$ and from Eq. (2.15), considering $\cos(\mathbf{n}, \mathbf{R}) = 1$,

$$\frac{\partial G}{\partial n} = \left(ik - \frac{1}{R}\right)\frac{e^{ikR}}{R} \approx ik\frac{e^{ikR}}{R} = ikG \ ,$$

for large R. The surface integral on S_R then reduces to

$$\iint\limits_{S_R}\left(G\frac{\partial U}{\partial n} - U\frac{\partial G}{\partial n}\right)\mathrm{d}s \approx \iint\limits_{S_R} G\left(\frac{\partial U}{\partial n} - ikU\right)\mathrm{d}s = \int\limits_{\Omega} G\left(\frac{\partial U}{\partial n} - ikU\right)R^2\mathrm{d}\Omega \ , \tag{2.19}$$

where Ω is the solid angle subtended by S_R at P_0. Here, the last step in Eq. (2.19) is nothing more than a simple transformation to spherical coordinates (see Appendix A). On a plane screen, we assume that the disturbance U satisfies the *Sommerfeld radiation condition*,

$$\lim_{R\to\infty} R\left(\frac{\partial U}{\partial n} - ikU\right) = 0 \ , \tag{2.20}$$

uniformly in angle, as R becomes arbitrarily large. This condition is used to eliminate inward propagating waves at infinity, so that we are guaranteed to have outward propagating waves only on S_R. Furthermore, since $|RG| = 1$ (using Eq. (2.18)), the entire integral over S_R in Eq. (2.19) vanishes as R approaches infinity, and hence Eq. (2.17) becomes

$$U(P_0) = \frac{1}{4\pi} \iint\limits_{S_P} \left(G \frac{\partial U}{\partial n} - U \frac{\partial G}{\partial n} \right) \mathrm{d}s \,. \tag{2.21}$$

Equation (2.21) allows us to express the disturbance at the observation point P_0 in terms of the disturbance and its normal derivative over the infinite plane S_P immediately behind the screen.

2.3 The Kirchhoff Boundary Conditions

As mentioned earlier, the screen is opaque except for the aperture which we denote as S_A, (see Figure 2.2). Intuitively one might think that the major contribution to the integral over S_P will come from the points that are located within the aperture S_A on S_P. Kirchhoff accordingly stated this in the following assumptions known as *Kirchhoff boundary conditions* [20, 21]:

i) Across the aperture S_A, the disturbance U and hence its derivative $\partial U/\partial n$ are exactly the same as they would be in the absence of the screen.

ii) Over the portion of S_P that lies in the shadow of the screen, *i.e.* $S_P \setminus S_A$, the disturbance U and its derivative $\partial U/\partial n$ are identically zero.

By neglecting the presence of the screen, the first condition allows us to specify the disturbance incident on the aperture whereas the second condition allows us to neglect all of the surface of integration except at the aperture S_A. Hence applying these boundary conditions to Eq. (2.21) yields

$$U(P_0) = \frac{1}{4\pi} \iint\limits_{S_A} \left(G \frac{\partial U}{\partial n} - U \frac{\partial G}{\partial n} \right) ds \,. \tag{2.22}$$

Here one should note that even though Kirchhoff boundary conditions simplify the result considerably, neither one of these conditions can exactly be true. It is inevitable that the presence of the screen will distort the unperturbed fields on S_A to some degree. Hence along the rim of the aperture, certain boundary conditions must be met that would not be required in the absence of the screen. Furthermore, the shadow behind the screen is never perfect since fields will inevitably extend behind the screen and diminish gradually over a wavelength. However, if the dimensions of the aperture, although small compared to the distances of both the observation point P_0 and the source point from the screen, are large compared to the wavelength, these so-called *fringing effects* can safely be neglected and these Kirchhoff boundary conditions give satisfactory results which are in good agreement with experimental observations [19, 20, 21, 22].

2.4 Rayleigh-Sommerfeld Formulation of Diffraction

Suppose we modify the Green's function of the Kirchhoff theory such that G or $\partial G/\partial n$ vanishes over the entire surface S_P while our approach leading to Eq. (2.22) remains valid. Such a modification removes the necessity of imposing the boundary conditions on both U and $\partial U/\partial n$ and the inconsistencies of the Kirchhoff theory are eliminated.

Let us now suppose that the function G is generated not only by a point source located at P_0, but also simultaneously by a second point source at $\tilde{P}_0$ which is the mirror image of P_0 on the opposite side of the screen, as illustrated in Figure 2.3. If we take the source at $\tilde{P}_0$ be of the same wavelength as the source at P_0, and suppose that the two sources are oscillating with a 180$^{\text{o}}$ phase difference, the resulting Green's function is given by

$$\tilde{G}(P_1) = \frac{e^{ikr_0}}{r_0} - \frac{e^{ik\tilde{r}_0}}{\tilde{r}_0}\,, \tag{2.23}$$

where $r_0 = |\mathbf{r_0}| = |\overrightarrow{P_0P_1}|$, $\tilde{r}_0 = |\tilde{\mathbf{r}}_\mathbf{0}| = |\overrightarrow{\tilde{P}_0P_1}|$. One can easily show that

$$\frac{\partial \tilde{G}(P_1)}{\partial n} = \cos(\mathbf{n}, \mathbf{r_0}) \left(ik - \frac{1}{r_0}\right) \frac{e^{ikr_0}}{r_0} - \cos(\mathbf{n}, \tilde{\mathbf{r}}_\mathbf{0}) \left(ik - \frac{1}{\tilde{r}_0}\right) \frac{e^{ik\tilde{r}_0}}{\tilde{r}_0}\,.$$

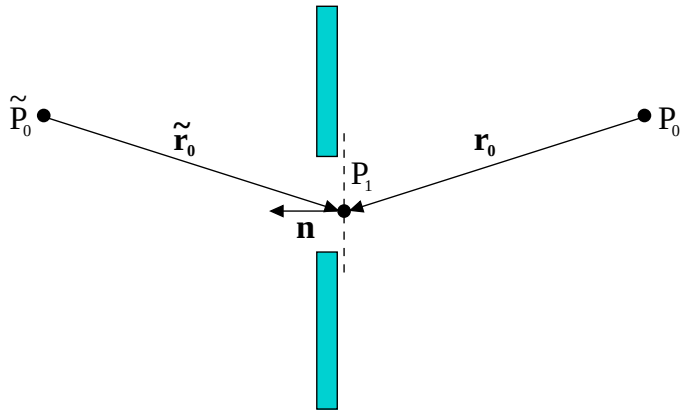

Figure 2.3: Mirror image of P_0 on the opposite side of a planar screen used in the derivation of Rayleigh-Sommerfeld Diffraction Formula.

At any point P_1 on S_P we have

$$r_0 = \tilde{r}_0\,, \quad \text{and} \quad \cos(\mathbf{n}, \mathbf{r_0}) = -\cos(\mathbf{n}, \tilde{\mathbf{r}}_\mathbf{0})$$

and therefore

$$\tilde{G}(P_1) = 0\,, \tag{2.24}$$

and

$$\frac{\partial \tilde{G}(P_1)}{\partial n} = 2\cos(\mathbf{n}, \mathbf{r_0}) \left(ik - \frac{1}{r_0}\right) \frac{e^{ikr_0}}{r_0}\,,$$

on the surface S_P. If we choose a coordinate system such that the screen S_P lies on the $z = 0$ plane, then it is easy to show that

$$\cos(\mathbf{n}, \mathbf{r_0}) = \frac{z_0}{r_0},$$

and

$$\frac{\partial \tilde{G}(P_1)}{\partial n} = 2\frac{z_0}{r_0} \left(ik - \frac{1}{r_0}\right) \frac{e^{ikr_0}}{r_0}\,. \tag{2.25}$$

As discussed earlier, the distance from the screen to the observation point P_0 is very large compared to the wavelength, *i.e.* $r_0 \gg \lambda$, and we therefore can re-write Eq. (2.25)

as

$$\frac{\partial \tilde{G}(P_1)}{\partial n} \approx -2ikz_0 \frac{e^{ikr_0}}{r_0^2}\,. \tag{2.26}$$

By substituting Eqs. (2.24) and (2.26) into Eq. (2.22)—which we obtained after applying the Kirchhoff boundary conditions for the Green's function G—we obtain the *first Rayleigh-Sommerfeld diffraction formula* for a single point source illuminating the aperture,

$$U(P_0) = \frac{z_0}{i\lambda} \iint\limits_{S_A} U(P_1) \frac{e^{ikr_0}}{r_0^2}\, ds\,, \tag{2.27}$$

or

$$U(x_0, y_0, z_0) = \frac{z_0}{i\lambda} \iint\limits_{S_A} U(x, y, 0) \frac{e^{ikr_0}}{r_0^2}\, dx\, dy\,. \tag{2.28}$$

The *intensity* of a scalar monochromatic wave at point P_0 is defined as the squared modulus of the complex amplitude $U(P_0)$ of the disturbance [20], is the given by

$$I(P_0) = |U(P_0)|^2 = \frac{z_0^2}{\lambda^2} \left| \iint\limits_{S_A} U(P_1) \frac{e^{ikr_0}}{r_0^2}\, ds \right|^2 . \tag{2.29}$$

It is important to note that both the Kirchoff solution and the Rayleigh-Sommerfeld solutions are essentially equivalent at sufficiently large distances away from the aperture, and deviations only occur close to the aperture. Despite the inconsistencies, Kirchoff theory is more general since it does not require diffracting screens to be planar [20].

2.5 The Angular Spectrum

It is also possible to formulate scalar diffraction theory in Fourier space. If the complex field distribution of a monochromatic disturbance is Fourier analyzed across any plane, the various spatial Fourier components can be identified as plane waves traveling in different directions away from that plane.

Let us consider a monochromatic wave incident, with sources on any negative z-plane, propagating in the positive z-direction to a parallel plane at distance z_0. The

complex, monochromatic scalar field $U(x, y, 0)$ given at the aperture S_A in Figure 2.2, can be represented by a two dimensional Fourier integral on $U(x, y, 0)$ [20] given by

$$U(x, y, 0) = \iint_{-\infty}^{\infty} \tilde{U}(k_x, k_y; 0)\, e^{i(k_x x + k_y y)}\, dk_x\, dk_y\,, \tag{2.30}$$

where the Fourier transform $\tilde{U}(k_x, k_y; 0)$ is as follows

$$\tilde{U}(k_x, k_y; 0) = \frac{1}{(2\pi)^2} \iint_{-\infty}^{\infty} U(x, y, 0)\, e^{-i(k_x x + k_y y)}\, dx\, dy\,. \tag{2.31}$$

Including the time dependence, $\tilde{U}(k_x, k_y; 0)\, e^{i(k_x x + k_y y + \omega t)}$, may be regarded as a plane wave at $z = 0$, propagating with the direction cosines α, β and γ, where the wave vector can be written as $\mathbf{k} = \frac{2\pi}{\lambda}(\alpha \mathbf{e_x} + \beta \mathbf{e_y} + \gamma \mathbf{e_z})$. $\tilde{U}(k_x, k_y; 0)$ is also called the *angular spectrum* of $U(x, y, 0)$ [20, 23].

Now consider the resulting field $U(x, y, z)$ that appears across a parallel plane at a distance z to the right of the aperture plane which is located at $z = 0$. Its two dimensional Fourier representation in terms of its angular spectrum can be written as

$$U(x, y, z) = \iint_{-\infty}^{\infty} \tilde{U}(k_x, k_y; z)\, e^{i(k_x x + k_y y)}\, dk_x\, dk_y\,, \tag{2.32}$$

and its angular spectrum $\tilde{U}(k_x, k_y; z)$ is given by

$$\tilde{U}(k_x, k_y; z) = \frac{1}{(2\pi)^2} \iint_{-\infty}^{\infty} U(x, y, z)\, e^{-i(k_x x + k_y y)}\, dx\, dy\,. \tag{2.33}$$

The complex amplitude $U(x, y, z)$ satisfies the Helmholtz equation, given by Eq. (2.10), at all source-free points

$$\nabla^2 U(x, y, z) + k^2 U(x, y, z) = 0\,.$$

Substitution of $U(x,y,z)$ in Eq. (2.32) into the Helmholtz equation yields

$$\int\!\!\int_{-\infty}^{\infty} \left[\frac{\partial^2 \tilde{U}(k_x,k_y;z)}{\partial z^2} + \left(k^2 - k_x^2 - k_y^2\right)\, \tilde{U}(k_x,k_y;z) \right] e^{i(k_x x + k_y y)}\, dk_x\, dk_y = 0\,. \qquad (2.34)$$

This is true for all waves only if the integrand is zero. Hence the angular spectrum $\tilde{U}$ satisfies the following differential equation,

$$\tilde{U}_{zz}(k_x,k_y;z) + k_z^2\, \tilde{U}(k_x,k_y;z) = 0\,, \qquad (2.35)$$

where

$$k_z^2 = k^2 - k_x^2 - k_y^2\,. \qquad (2.36)$$

An elementary solution of this differential equation can be given by

$$\tilde{U}(k_x,k_y;z) = \tilde{U}(k_x,k_y;0)\, e^{-ik_z z} \qquad (2.37)$$

in which the down-going waves were ignored for simplicity. Note that $k_z = \sqrt{k^2 - k_x^2 - k_y^2}$ is real valued if $k_x^2 + k_y^2 < k^2$ and each angular spectrum component is just modified by a phase factor $e^{-ik_z z}$.

The relation we found between $\tilde{U}(k_x,k_y;z)$ and $\tilde{U}(k_x,k_y;0)$ in Eq. (2.37) now allows us to describe the wave field at (x,y,z) in terms of the initial angular spectrum, *i.e.*,

$$U(x,y,z) = \int\!\!\int_{-\infty}^{\infty} \tilde{U}(k_x,k_y;0)\, e^{i(k_x x + k_y y - k_z z)}\, dk_x\, dk_y\,. \qquad (2.38)$$

2.6 Summary

In this chapter we reviewed the scalar diffraction theory and introduced some of the definitions. We gave a short introduction to electromagnetic theory in Section 2.1. In Section 2.2 we derived the Helmholtz equation and showed that U satisfies the equation at all source-free points, and, then converted it into the Helmholtz-Kirchhoff Integral

equation by using the Green's theorem. Later we discussed the application of this integral for diffraction by a plane screen. In Section 2.3, we discussed the Kirchhoff boundary conditions. We then removed the inconsistencies of the Kirchhoff theory by reformulating the problem using Rayleigh-Sommerfeld theory of diffraction. Finally, we introduced the angular spectrum of the incident wave and described the wave field in terms of initial angular spectrum. We will use this description in the following Chapter where we discuss the forward problem.

Chapter 3

Forward Problem

In this chapter, we introduce the forward problem for which we investigate the intensity output, given the mask. We introduce a mask function by which we define the mask structure. The mask function allows us to write the transmitted field at the mask, and using the angular spectrum we obtain the transmitted field at the image plane, namely the silicon wafer used in production (see Chapter 1). We then discuss the Hopkins theory of partially coherent imaging [22, 24], which uses transmission cross coefficients (TCC) to calculate the image intensity pattern. We employ the technique that was described by Cobbs [2], called *Sum of Coherent Systems* (SOCS). We use this technique because of the partial linearity of the resulting system approximation. The use of decompositions to Hopkins imaging equations are found in the literature extensively [25, 26]. In this method the TCC are first obtained as a matrix, then the Singular Value Decomposition (SVD) algorithm is applied to obtain optical kernels of the system. Then, in order to obtain an optimal approximation to Hopkins equation, the system is truncated to a low order.

The organization of the chapter is as follows. In Section 3.1 we state the forward problem in detail, followed by a derivation of the aerial image intensity using the Hopkins' model in Section 3.2. In Section 3.3 numerical calculation of the coherent point spread function is discussed, and some numerical results for the aerial intensity calculation are shown. We give a summary of the chapter in Section 3.4.

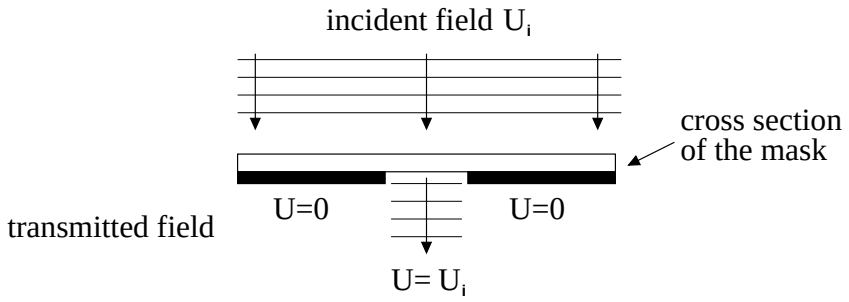

Figure 3.1: Kirchoff boundary conditions for the near field of mask.

3.1 The Statement of the Forward Problem

Assume that an opaque screen containing a structure of apertures, namely the *mask*, is introduced in the plane $z = 0$. Let us consider the effects of the mask on the angular spectrum of the incident field. We define a binary *mask function*, $m(x, y)$, of an aperture structure under Kirchhoff boundary conditions, such that the transmitted field amplitude $U(x, y; 0)$ at any (x, y) point across the aperture in the $z = 0$ plane is given by

$$U(x, y, 0) = U_i(x, y, 0)\, m(x, y)\,. \tag{3.1}$$

Here, $U_i(x, y, 0)$ is the complex amplitude of the incident field (see Figure 3.1). Mask function m takes the value "one" where there is an aperture and takes the value "zero" at the screen. The Kirchhoff boundary conditions are therefore satisfied. Kirchhoff approximation for the near field of mask ignores scattering and it is only accurate in the middle of large uniform areas. For a single plane incident wave at $z = 0$, we can write

$$U_i(x, y, 0) = e^{i\left(k_x^{(i)} x + k_y^{(i)} y\right)}\,. \tag{3.2}$$

In order to describe the wave field at the image plane in terms of the initial spectrum, given by Eq. (2.38), we need the Fourier transform of $U(x, y, 0)$. It follows once from

Eq. (2.31) and Eq. (3.1) that angular spectrum of $U(x, y, 0)$ is

$$\tilde{U}(k_x, k_y; 0) = \frac{1}{(2\pi)^2} \iint_{-\infty}^{\infty} U_i(x, y, 0)\, m(x, y)\, e^{-i(k_x x + k_y y)}\, dx\, dy\,. \tag{3.3}$$

Replacing $m(x, y)$ with its inverse Fourier transform and by substituting Eq. (3.2), we can write Eq. (3.3) as

$$\tilde{U}(\mathbf{k}_\perp; 0) = \frac{1}{(2\pi)^2} \iint_{-\infty}^{\infty} \left(\iint_{-\infty}^{\infty} \tilde{m}(\bar{\mathbf{k}}_\perp) e^{i(\bar{\mathbf{k}}_\perp \cdot \mathbf{r})}\, d\bar{\mathbf{k}}_\perp \right) e^{i\left(\mathbf{k}_\perp^{\mathbf{i}} - \mathbf{k}_\perp\right) \cdot \mathbf{r}_\perp}\, d\mathbf{r}_\perp\,, \tag{3.4}$$

where $\tilde{m}(\bar{\mathbf{k}}_\perp)$ denotes the Fourier transform of $m(x, y)$. Here and in the remaining of this chapter, we use, for brevity, the vector notation $\mathbf{k}_\perp$ and $\mathbf{r}_\perp$ to denote (k_x, k_y) and (x, y), respectively. By re-arranging the terms in the integrand and using the Fourier representation of the two-dimensional delta function, *i.e.*,

$$\delta(\mathbf{k}_\perp^{\mathbf{i}} - \mathbf{k}_\perp + \bar{\mathbf{k}}_\perp) = \frac{1}{(2\pi)^2} \iint_{-\infty}^{\infty} e^{i(\mathbf{k}_\perp^{\mathbf{i}} - \mathbf{k}_\perp + \bar{\mathbf{k}}_\perp) \cdot \mathbf{r}_\perp}\, d\mathbf{r}_\perp\,, \tag{3.5}$$

we obtain

$$\tilde{U}(\mathbf{k}_\perp; 0) = \iint_{-\infty}^{\infty} \tilde{m}(\bar{\mathbf{k}}_\perp) \delta(\mathbf{k}_\perp^{\mathbf{i}} - \mathbf{k}_\perp + \bar{\mathbf{k}}_\perp)\, d\bar{\mathbf{k}}_\perp = \tilde{m}(\mathbf{k}_\perp - \mathbf{k}_\perp^{\mathbf{i}})\,. \tag{3.6}$$

Here we used the shifting property of delta function which is given by

$$\iint_{-\infty}^{\infty} f(\mathbf{x}) \delta\left(\mathbf{x} - \mathbf{x_0}\right)\, d\mathbf{x} = f(\mathbf{x_0})\,.$$

Hence by substituting Eq. (3.6) into Eq. (2.38) we obtain the propagated near field

$$U(\mathbf{r}_\perp, z; \mathbf{k}_\perp^{\mathbf{i}}) = \iint_{-\infty}^{\infty} \tilde{m}(\mathbf{k}_\perp - \mathbf{k}_\perp^{\mathbf{i}})\, e^{i(\mathbf{k}_\perp \cdot \mathbf{r}_\perp - k_z z)}\, d\mathbf{k}_\perp\,. \tag{3.7}$$

If we take into account that the field propagates through a lens, the field at the image plane could be written as

$$U(\mathbf{r}_\perp, z; \mathbf{k}^{\mathbf{i}}_\perp) = \iint_{-\infty}^{\infty} \tilde{m}(\mathbf{k}_\perp - \mathbf{k}^{\mathbf{i}}_\perp)\, P(\mathbf{k}_\perp)\, e^{i(\mathbf{k}_\perp \cdot \mathbf{r}_\perp - k_z z + kW(\mathbf{k}_\perp))}\, d\mathbf{k}_\perp \,, \tag{3.8}$$

where $P(\mathbf{k}_\perp)$ and $W(\mathbf{k}_\perp)$ denote *the pupil function* and *the lens aberration*, respectively. As mentioned in Chapter 1, these aberrations are typically caused by the imperfections in the lenses. Aberrations result in wavefronts with a phase error, typically represented by $kW(\mathbf{k}_\perp)$ [20]. One can therefore see that W is an effective path-length error. For simplicity, however, we assume an optical system that is aberration-free, *i.e.* $W(\mathbf{k}_\perp) = 0$. We also assume that a circular pupil is used and hence the pupil function $P(\mathbf{k}_\perp)$ is given by

$$P(\mathbf{k}_\perp) \equiv circ(\mathbf{k}_\perp) = \begin{cases} 1 & |\mathbf{k}_\perp| \leq k \\ 0, & |\mathbf{k}_\perp| > k \,. \end{cases} \tag{3.9}$$

Equation (3.9) will be frequently used in the calculations of the coherent point spread function and the image intensities in Section 3.3.

3.2 The Hopkin's Model

In this section, we derive the aerial image intensity using the Hopkin's theory. Aerial image is the pattern on the top of the resist that is produced by the incident wave. For modeling aerial images under partially coherent illumination one needs to superimpose the effect of each illumination source that makes up the partially coherent source. The aerial image intensity, I, is therefore given by an integral over the incident wave vectors $\mathbf{k}^{\mathbf{i}}_\perp$, *i.e.*

$$I(\mathbf{r}_\perp, z) = \iint_{\mathbf{k}^{\mathbf{i}}_\perp \text{ in the illuminator pupil}} \left| U(\mathbf{r}_\perp, z; \mathbf{k}^{\mathbf{i}}_\perp) \right|^2 \mathcal{P}(\mathbf{k}^{\mathbf{i}}_\perp) d\mathbf{k}^{\mathbf{i}}_\perp \,, \tag{3.10}$$

which is also known as the Abbe representation [27]. Here $\mathcal{P}(\mathbf{k}^{\mathbf{i}}_\perp)$ is known as *the pupil illumination function.*

We know that

$$\left|U(\mathbf{r}_\perp, z; \mathbf{k}^{\mathbf{i}}_\perp)\right|^2 = U(\mathbf{r}_\perp, z; \mathbf{k}^{\mathbf{i}}_\perp)\, U^*(\mathbf{r}_\perp, z; \mathbf{k}^{\mathbf{i}}_\perp)\,, \tag{3.11}$$

where asteriks denotes the complex conjugate. By substituting Eqs. (3.7) and (3.11) into Eq. (3.10), one can write for the aerial image intensity

$$\begin{aligned} I(\mathbf{r}_\perp, z) \;=\; & \iint d\mathbf{k}^{\mathbf{i}}_\perp\, \mathcal{P}(\mathbf{k}^{\mathbf{i}}_\perp) \iint d\mathbf{k}'_\perp \iint d\mathbf{k}''_\perp\, e^{i\left(\mathbf{k}'_\perp\cdot\mathbf{r}_\perp - k'_z z\right)}\, \tilde{m}(\mathbf{k}'_\perp - \mathbf{k}^{\mathbf{i}}_\perp) circ(\mathbf{k}'_\perp) \\ & \times e^{-i\left(\mathbf{k}''_\perp\cdot\mathbf{r}_\perp - k''_z z\right)}\, \tilde{m}^*(\mathbf{k}''_\perp - \mathbf{k}^{\mathbf{i}}_\perp) circ(\mathbf{k}''_\perp)\,. \end{aligned} \tag{3.12}$$

Here and in the following, we omit the integral limits $(-\infty, \infty)$ to simplify the notation. Using the Fourier transform of $m(\mathbf{r}_\perp)$,

$$\tilde{m}(\mathbf{k}_\perp) = \frac{1}{(2\pi)^2} \iint m(\mathbf{r}_\perp) e^{-i(\mathbf{k}_\perp\cdot\mathbf{r}_\perp)} d\mathbf{r}_\perp\,, \tag{3.13}$$

yields

$$\begin{aligned} I(\mathbf{r}_\perp, z) \;=\; & \frac{1}{(2\pi)^4} \iint d\mathbf{r}'_\perp \iint d\mathbf{r}''_\perp\, m^*(\mathbf{r}''_\perp)\, K^*(\mathbf{r}_\perp - \mathbf{r}''_\perp; z)\, K(\mathbf{r}_\perp - \mathbf{r}'_\perp; z)\, m(\mathbf{r}'_\perp) \\ & \times \iint d\mathbf{k}^{\mathbf{i}}_\perp\, e^{i\mathbf{k}^{\mathbf{i}}_\perp\cdot\left(\mathbf{r}'_\perp - \mathbf{r}''_\perp\right)} \mathcal{P}(\mathbf{k}^{\mathbf{i}}_\perp)\,. \end{aligned} \tag{3.14}$$

Here,

$$K(\mathbf{r}_\perp; z) \equiv \iint d\mathbf{k}_\perp e^{i(\mathbf{k}_\perp\cdot\mathbf{r}_\perp - k_z z)} circ(\mathbf{k}_\perp)\,, \tag{3.15}$$

is called *the coherent point-spread function* and it describes properties of the imaging system [12]. Furthermore, by defining

$$J(\mathbf{r}_\perp) \equiv \iint d\mathbf{k}^{\mathbf{i}}_\perp e^{i\mathbf{k}^{\mathbf{i}}_\perp\cdot\mathbf{r}_\perp}\, \mathcal{P}(\mathbf{k}^{\mathbf{i}}_\perp)\,, \tag{3.16}$$

as *the mutual intensity function*, which describes coherence properties of the illumination

[12], one gets

$$I(\mathbf{r}_\perp, z) = \frac{1}{(2\pi)^4} \iint d\mathbf{r}'_\perp \iint d\mathbf{r}''_\perp \, m^*(\mathbf{r}''_\perp) \, K^*(\mathbf{r}_\perp - \mathbf{r}''_\perp) \, J(\mathbf{r}'_\perp - \mathbf{r}''_\perp) \, K(\mathbf{r}_\perp - \mathbf{r}'_\perp) \, m(\mathbf{r}'_\perp) \, . \tag{3.17}$$

If we then re-define $\mathbf{r}'_\perp \rightarrow \mathbf{r}_\perp - \mathbf{r}'_\perp$ and $\mathbf{r}''_\perp \rightarrow \mathbf{r}_\perp - \mathbf{r}''_\perp$, we obtain the aerial image intensity in the spatial domain as

$$I(\mathbf{r}_\perp, z) = \frac{1}{(2\pi)^4} \iint d\mathbf{r}'_\perp \iint d\mathbf{r}''_\perp \, m^*(\mathbf{r}_\perp - \mathbf{r}''_\perp) \underbrace{\left[K^*(\mathbf{r}''_\perp; z) \, J(\mathbf{r}''_\perp - \mathbf{r}'_\perp) \, K(\mathbf{r}'_\perp; z)\right]}_{H} m(\mathbf{r}_\perp - \mathbf{r}'_\perp) \, . \tag{3.18}$$

The form shown in Eq. (3.18) is also known as Hopkins model [22, 28] . Hopkins model is based on the exchange of the integration order over the point source contributions and the diffraction amplitudes. Let us define the term in square brackets in Eq. (3.18), *i.e.*

$$H(\mathbf{r}'_\perp, \mathbf{r}''_\perp; z) \equiv K^*(\mathbf{r}''_\perp; z) \, J(\mathbf{r}''_\perp - \mathbf{r}'_\perp) \, K(\mathbf{r}'_\perp; z) \, , \tag{3.19}$$

as the Hopkins transmission cross coefficients (TCC) function for the calculations of the aerial image intensity [27]. In other words, the discrete Hopkins expansion is simply an expression of the transmission cross coefficient function as a tensor product. Such a definition has the advantage that a given optical system with fixed illumination, numerical aperture, defocus, and other aberrations can be easily described and that the TCC need to be calculated only once and these results can be used again for aerial image calculation of different mask patterns [27].

First, let us look into the calculation of $J(\mathbf{r}_\perp)$ in Eq. (3.16). Commonly the pupil illumination function, which is also known as the Fourier transform of the mutual intensity function, $\mathcal{P}(\mathbf{k}^\mathbf{i}_\perp)$ is chosen as follows [2] :

$$\mathcal{P}(\mathbf{k}^\mathbf{i}_\perp) = \begin{cases} \dfrac{\lambda^2}{\pi s^2 (NA)^2}, & |\mathbf{k}^\mathbf{i}_\perp|^2 < \dfrac{s^2 (NA)^2}{\lambda^2} \\ 0, & |\mathbf{k}^\mathbf{i}_\perp|^2 > \dfrac{s^2 (NA)^2}{\lambda^2} \end{cases} , \tag{3.20}$$

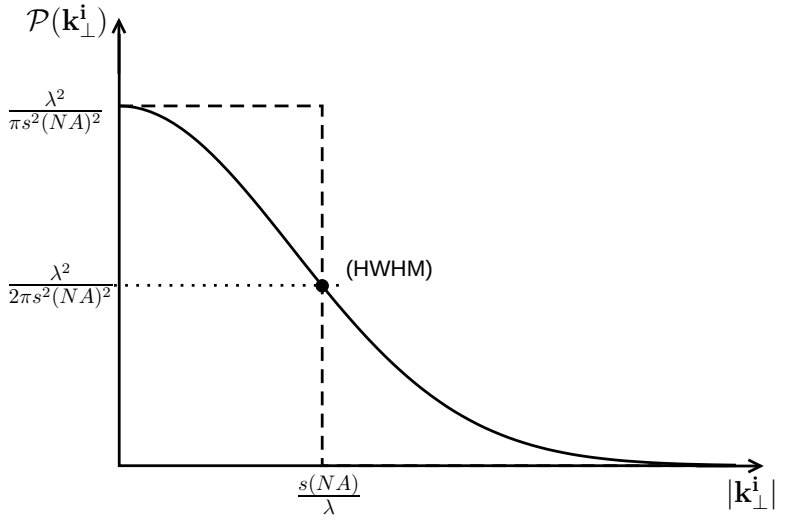

Figure 3.2: The pupil illumination function approximated by a Gaussian form. We set the half width at half maximum (HWHM) of the Gaussian curve equal to the half of the maximum of Eq. (3.20).

where s is the partial coherence factor given by

$$s = \frac{NA \text{ of condenser}}{NA \text{ of imaging optics}}\,. \tag{3.21}$$

We approximate the pupil illumination function with a Gaussian form

$$\mathcal{P}(\mathbf{k}_\perp^{\mathbf{i}}) = \mathcal{P}_0\, e^{-\beta|\mathbf{k}_\perp^{\mathbf{i}}|^2}\,, \tag{3.22}$$

as illustrated in Figure 3.2. It is straightforward to show that $\mathcal{P}_0 = \dfrac{\lambda^2}{\pi s^2(NA)^2}$ and by using the HWHM value

$$P\left(\frac{sNA}{\lambda}\right) = \frac{1}{2}\frac{\lambda^2}{\pi s^2(NA)^2}\,, \tag{3.23}$$

one finds

$$\beta = \frac{\lambda^2 \ln 2}{s^2(NA)^2}\,. \tag{3.24}$$

Equation (3.16) in one dimension then becomes

$$J(x) \equiv \frac{\lambda}{\sqrt{\pi} s(NA)} \int e^{\left(i k_x x - \frac{\lambda^2 \ln 2}{s^2 (NA)^2} k_x^2 \right)} dk_x = \frac{1}{\sqrt{\ln 2}} e^{-\frac{s^2 (NA)^2}{4 \lambda^2 \ln 2} x^2} . \tag{3.25}$$

Hence in two dimensions $J(\mathbf{r}_\perp)$ is found to be

$$J(\mathbf{r}_\perp) = \frac{1}{\ln 2} \, e^{-|\mathbf{r}_\perp|^2 / 4\beta} . \tag{3.26}$$

This calculation also shows that the mutual intenstiy function J is a real valued function. With this result one can show that $H(\mathbf{r}'_\perp, \mathbf{r}''_\perp; z)$ in Eq. (3.19) is a positive, semi-definite hermitian operator [2], *i.e.*

$$H^*(\mathbf{r}''_\perp, \mathbf{r}'_\perp; z) = \left[K^*(\mathbf{r}'_\perp; z) \, J(\mathbf{r}'_\perp - \mathbf{r}''_\perp) \, K(\mathbf{r}''_\perp; z) \right]^* = H(\mathbf{r}'_\perp, \mathbf{r}''_\perp; z) . \tag{3.27}$$

Since digital images are essentially matrices, we have to work in discretized coordinates. For an image of size $L_x \times L_y$, H can be written as

$$H(\mathbf{r}'_\perp = i \, \Delta x \mathbf{e_x} + j \, \Delta y \mathbf{e_y}, \mathbf{r}''_\perp = i' \, \Delta x \mathbf{e_x} + j' \, \Delta y \mathbf{e_y}; z) \equiv H(i, j, i', j') , \tag{3.28}$$

where $\Delta x = L_x / N$ and $\Delta y = L_y / N$ with $i, j, i', j' = 1, \ldots N$. For brevity in notation, we omit the z dependence of H. We can represent the discretized H as a matrix by defining a linear mapping $\mathcal{H} : \mathbb{R}^{N \times N} \longmapsto N \times N$;

$$[\tilde{H}(X)]_{i,j} = \sum_{i'=1}^{N} \sum_{j'=1}^{N} H(i, j, i', j') X_{i', j'} \tag{3.29}$$

for a given matrix $X \in \mathbb{R}^{N \times N}$. This is performed first by stacking the columns of matrix as a vector from $\mathbb{R}^{N^2}$ and then writing the operation as a matrix vector multiplication.

The column stacking function $\mathcal{C} : R^{N \times N} \longmapsto R^{N^2}$ is defined by

$$\mathcal{C}(X_{i,j}) = \mathcal{X}_{j \times N + i} , \tag{3.30}$$

where X is an $N \times N$ matrix. That is, for

$$X = \begin{bmatrix} x_{11} & x_{12} & \dots & x_{1N} \\ x_{21} & x_{22} & \dots & x_{2N} \\ \vdots & \vdots & \ddots & \vdots \\ x_{N1} & x_{N2} & \dots & x_{NN} \end{bmatrix} = \begin{bmatrix} \mathbf{x}_1 & \mathbf{x}_2 & \dots & \mathbf{x}_N \end{bmatrix}. \tag{3.31}$$

the column stacking operation yields

$$\mathcal{X} = \mathcal{C}(X) = \begin{bmatrix} \mathbf{x}_1 \\ \mathbf{x}_2 \\ \vdots \\ \mathbf{x}_N \end{bmatrix}. \tag{3.32}$$

The operator $\tilde{H}$ can be represented as a matrix, $\mathcal{H}$,

$$\mathcal{H} = \begin{bmatrix} H(1,1,1,1) & H(1,1,2,1) & \dots & H(1,1,N,1) & H(1,1,1,2) & \dots & H(1,1,N,N) \\ H(2,1,1,1) & H(2,1,2,1) & & & & & H(2,1,N,N) \\ \vdots & \vdots & \ddots & & & & \vdots \\ H(N,1,1,1) & H(N,1,2,1) & & & & & H(N,1,N,N) \\ H(1,2,1,1) & \vdots & & & & & \vdots \\ H(2,2,1,1) & & & & & & \\ \vdots & & & & & & \\ H(N,2,1,1) & & & & & & \\ \vdots & \vdots & & & & \ddots & \vdots \\ H(N,N,1,1) & H(N,N,2,1) & \dots & & & \dots & H(N,N,N,N) \end{bmatrix}, \tag{3.33}$$

operating on the stacked vector $\mathcal{X}$. We then apply singular value decomposition (SVD) to decompose H into its eigenspectrum. However, since TCC matrix is positive semi-definite hermitian matrix, SVD is equivalent to an eigenfunction expansion [29]

$$\mathcal{H} = \sum_{n=1}^{N} \sigma_n \mathcal{V}_n \mathcal{V}_n^*, \tag{3.34}$$

(for more details please also see B.1). Furthermore, the eigenvectors of $\mathcal{H}$ form a complete orthonormal basis and the eigenvalues are real and non-negative [30]. The inverse column stacking operation then yields

$$V_n = \mathcal{C}^{-1}(\mathcal{V}_n)\,. \tag{3.35}$$

Hence one can write

$$H(\mathbf{r}'_\perp, \mathbf{r}''_\perp; z) \approx \sum_{n=1} \sigma_n V_n V_n^*\,, \tag{3.36}$$

where $\{\sigma_n\}$ and $\{V_n\}$ are the non-negative eigenvalues and the corresponding eigenfunctions of the Hermitian operator H, respectively. However, it has been shown that the eigenvalues decrease rapidly to zero [2]. Hence the summation given in Eq. (3.36) is dominated by the first several terms, for the eigenvectors sorted in descending order $\sigma_1 \geq \sigma_2 \geq \cdots \geq \sigma_{N^2}$. The series therefore could be truncated after few terms as follows

$$H(\mathbf{r}'_\perp, \mathbf{r}''_\perp; z) \approx \sum_{n=1}^{N_t} \sigma_n V_n V_n^*\,, \tag{3.37}$$

where N_t denotes maximum number of terms that are used for the approximation. The intensity in Eq. (3.18) then can be written as

$$I(\mathbf{r}_\perp; z) = \sum_{n=1}^{N_t} \sigma_n \, |(V_n \star m)(\mathbf{r}_\perp; z)|^2 = \sum_{n}^{N_t} \sigma_n \, \left| \iint d\mathbf{r}'_\perp \, V_n(\mathbf{r}'_\perp - \mathbf{r}_\perp; z)\, m(\mathbf{r}'_\perp) \right|^2 \,, \tag{3.38}$$

where $\star$ denotes two-dimensional convolution. Hence with this decomposition, the computation of the image intensity is reduced to a two-dimensional convolution. To summarize, we showed that the overall aerial image intensity matrix of the partially coherent optical system can be approximated by a finite sum of the image matrices produced by coherent systems.

3.3 Numerical Calculations

Calculation of the Coherent Point Spread Function, $K(\mathbf{r}_\perp; z)$

In order to calculate the integral given by Eq. (3.15) we use polar coordinates,*i.e.* $k_x = |\mathbf{k}_\perp| \cos\phi$ and $k_y = |\mathbf{k}_\perp| \sin\phi$, and obtain

$$K(\mathbf{r}_\perp; z) = \int_0^\infty \int_0^{2\pi} \exp\{\, i\,|\mathbf{k}_\perp|\, x\, \cos\phi + i\,|\mathbf{k}_\perp|\, y \sin\phi - i\, k_z\, z\}\, circ(\mathbf{k}_\perp)\, |\mathbf{k}_\perp|\, d\phi\, d|\mathbf{k}_\perp|\,, \tag{3.39}$$

where $k_z = \sqrt{k^2 - \mathbf{k}_\perp^2}$ as discussed in Section 2.5. We also know that k_z would be real valued under the condition of $|\mathbf{k}_\perp| < k$ (using the definition of *circ* function). Under this assumption the integral above becomes

$$K(\mathbf{r}_\perp; z) = K(x, y; z) = \int_0^k \int_0^{2\pi} \exp\{\, i\,|\mathbf{k}_\perp|\, x\, \cos\phi + i\,|\mathbf{k}_\perp|\, y \sin\phi - i\, k_z\, z\}\; |\mathbf{k}_\perp|\, d\phi\, d|\mathbf{k}_\perp|\,. \tag{3.40}$$

Note that, If $z = 0$ one can represent Eq. (3.40) as *Jinc* function. However, for $z \neq 0$ one can approximate this integral by applying the *composite trapezoidal rule* given by Eq. (B.10) (see Appendix B.2 for details), namely

$$K(\mathbf{r}_\perp; z) \approx \frac{\Delta|\mathbf{k}_\perp|\, \Delta\phi}{4} \sum_{i=1}^{N+1} \sum_{j=1}^{M+1} w_{i,j}\, \mathcal{F}(\mathbf{r}_\perp, |\mathbf{k}_\perp|_i, \phi_j; z)\,, \tag{3.41}$$

to numerically evaluate $K(\mathbf{r}_\perp; z)$ in Eq. (3.40). Here $w_{i,j}$ are the weighting coefficients, $\Delta|\mathbf{k}_\perp| = k/N$ and $|\mathbf{k}_\perp|_i = (i-1)\,\Delta|\mathbf{k}_\perp|$, for $i = 1, 2, \ldots, (N+1)$, $\Delta\phi = 2\pi/M$ and $\phi_j = (j-1)\,\Delta\phi$, for $j = 1, 2, \ldots, M$ and

$$\mathcal{F}(\mathbf{r}_\perp, |\mathbf{k}_\perp|_i, \phi_j; z) = \exp\left\{ i\,|\mathbf{k}_\perp|_i (\, x\, \cos\phi_j + y\, \sin\phi_j) - i\, z \sqrt{k^2 - |\mathbf{k}_\perp|_i^2} \right\} |\mathbf{k}_\perp|_i\,. \tag{3.42}$$

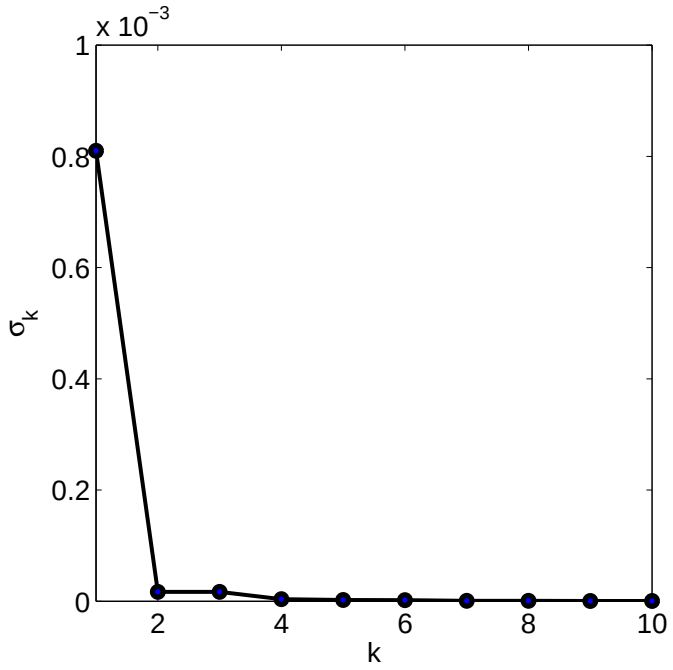

Figure 3.3: Eigenvalues σ_k obtained using the singular value decomposition for parameters $z = 0$, $\lambda = 193\ nm,\ s = 0.5,\ NA = 0.85$, and $N = 128$.

Singular Value Decomposition of $H(\mathbf{r}'_\perp, \mathbf{r}''_\perp; z)$

In order to obtain the eigenvalues and the corresponding eigenfunctions shown in Eq. (3.37) we used the "*eigs*" command in MATLAB which is based on the Arnoldi iteration method. In general "*eigs*" command is used to find largest eigenvalues and eigenvectors of a sparse matrix. Note that the eigenfunctions we need are $N \times N$ matrices. Therefore we used the column stacking operation that we described in Section 3.2 to define a function in the form of $y = fun(x)$ that is needed to use "*eigs*" command in the form of $d = eigs(fun, n, k, sigma, options)$ as it was given in Matlab "*eigs*" documentation. n is N^2 so that stacking method is used, and for the given k number "*eigs*" command returns the k many largest magnitude eigenvalues.

Numerical Intensity Calculation Results

In Figure 3.3, the first ten largest magnitude eigenvalues that are obtained after performing singular value decomposition for $z = 0$, $\lambda = 193\ nm$, $s = 0.5$, $NA = 0.85$, and $N = 128$ are shown. As expected, the eigenvalues decay rapidly, therefore, our assumption of truncating the series given in Eq. (3.37) is justified. Here and in the remainder of the thesis we used the first ten eigenvalues in our calculations. Figure 3.4 shows the first six kernels corresponding to these eigenvalues for $z = 0$, $\lambda = 193\ nm$, $s = 0.5$, $NA = 0.85$, and $N = 128$. These results are in good agreement with that of shown in [2, 31]. Note that these eigenvalues and eigenfunctions are needed to be calculated only once for specific z, λ, NA, s, and N values and then one could use any desired mask pattern to calculate the intensity using Eq. (3.38).

In order to see the final aerial image patterns, we designed two different masks as shown in Figures 3.5 (top) and 3.6 (top). Some of the features in these masks are especially chosen to illustrate the interactions between close elements. The resulting aerial image intensities are shown in Figures 3.5 (bottom) and 3.6 (bottom) for $z = 0$, $\lambda = 193\ nm$, $s = 0.5$, $NA = 0.85$, and $N = 256$. As can be seen from these images, when mask designs become complicated, it becomes harder to resolve the small features. Therefore, it is crucial to come up with better ways to accurately imprint mask designs on these substrates.

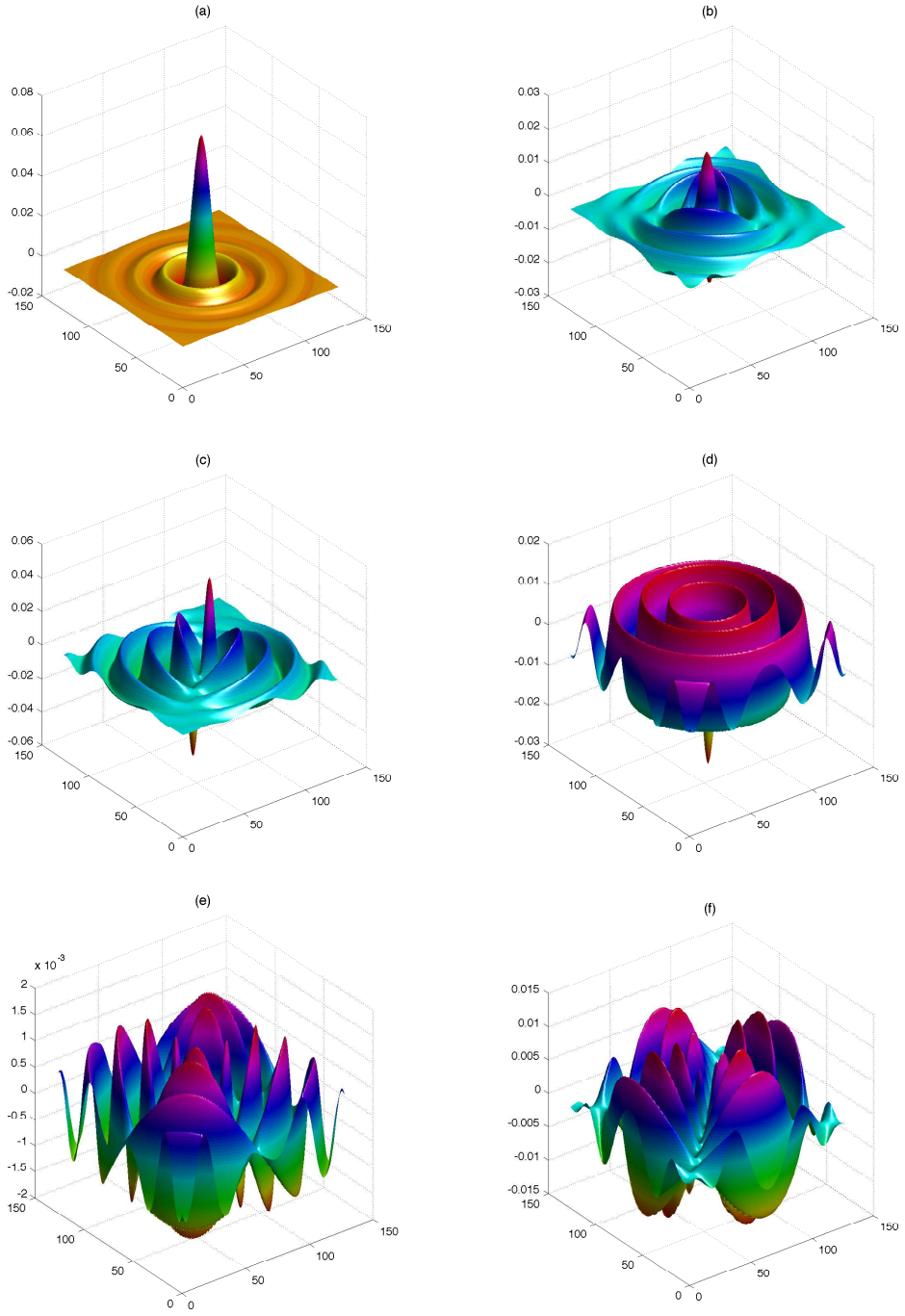

Figure 3.4: First six optical kernels (eigenfunctions), from (a) to (f), for a partially coherent system with parameters $z = 0$, $\lambda = 193\ nm$, $s = 0.5$, $NA = 0.85$, and $N = 128$.

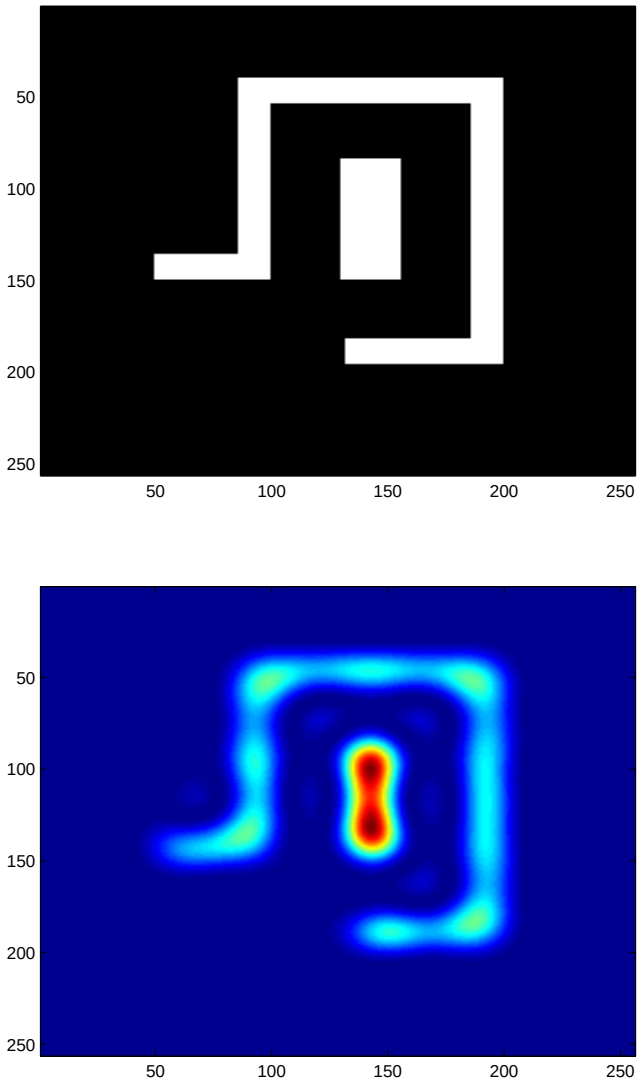

Figure 3.5: An example mask (top) that is used as the mask function m to obtain the aerial image intensity (bottom). Parameters: $z = 0$, $s = 0.5$, $\lambda = 193\ nm$, $NA = 0.85$, and $N = 256$.

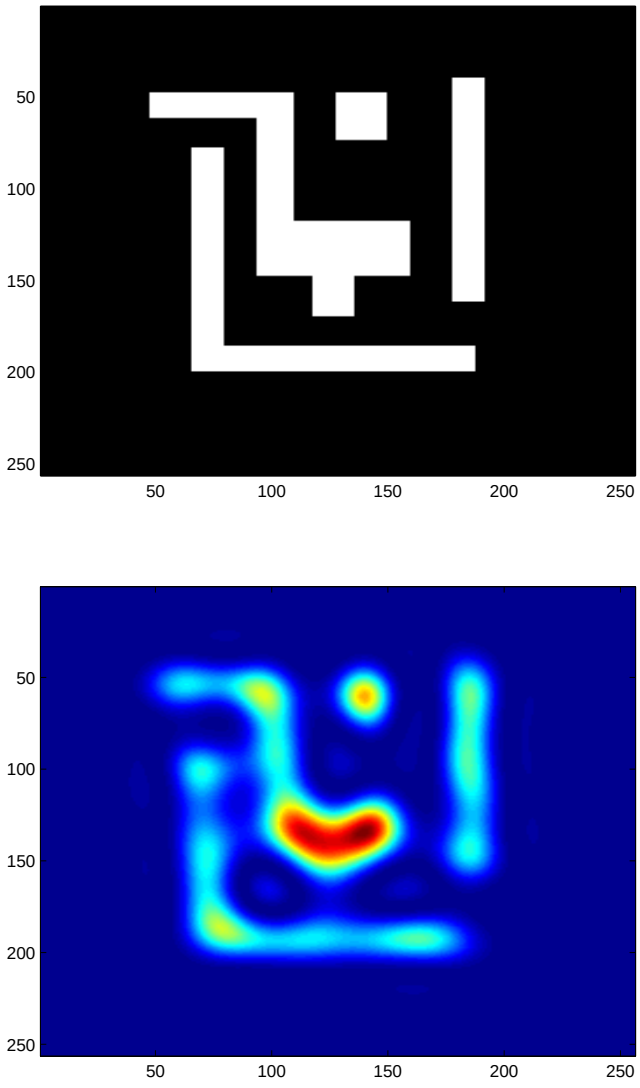

Figure 3.6: An example mask (top) that is used as the mask function m to obtain the aerial image intensity (bottom). Parameters: $z = 0$, $s = 0.5$, $\lambda = 193\ nm$, $NA = 0.85$, and $N = 256$.

3.4 Summary

In this chapter, we introduced the forward problem, that is, for any desired pattern find the aerial image intensity output. We used a mask function that allowed us to write the transmitted field at the mask, and using the angular spectrum we obtained the transmitted field at the image plane. We then discussed the Hopkins theory of partially coherent imaging that uses TCC to calculate the image intensity pattern by representing our partially coherent system as finite the sum of image matrices produced by coherent imaging systems. TCC are first obtained as a matrix, then the SVD algorithm is applied to obtain optical kernels of the system. We used MATLAB to calculate these singular values, and the optical kernels for commonly used set of parameters in the literature. These singular values, and optical kernels will be necessary to calculate each aerial image intensity when we introduce a level set formulation of inverse problem in the next chapter.

Chapter 4

The Inverse Problem

In this chapter, we begin by defining the inverse problem of mask design and the level set formulation of the forward problem. We the give a preliminary on volume and surface integrals in Section 4.2. These results will then be used in the calculations of Section 4.3. In Section 4.3, by calculating the variation of the cost function we show that the problem is equivalent of solving a Hamilton-Jacobi equation. We then review the standard Level Set Methods, introduced in [32], and Fast Marching Methods (FMM) [33], for tracking propagating interfaces in two and three dimensions, in Section 4.4. Both sets of techniques are based on a partial differential equations view of interface motion, and rely on the use of the theory of viscosity solutions, upwind schemes for hyperbolic conservation laws, and the theory of curve and surface evolution developed in [34]. In Section 4.5, we discuss the numerical results for different target mask layouts. Finally, in Section 4.6, we give a summary of the chapter.

4.1 The Inverse Problem for Mask Design

Problem statement: Given a binary target mask pattern $T(x, y)$ we would like to find a binary function $m(x, y)$ such that the pattern on the exposed region $S(x, y)$ is close to the target pattern.

Here we define the *exposed region* as the set of points such that the aerial image intensity $I(x, y; z)$ given by Eq. (3.38) is greater than some prescribed threshold $\mathcal{T}$ (the

intensity threshold required for the photoresist to react),

$$\mathcal{D} = \{(x, y) \ : \ I(x, y; z) > \mathcal{T}\}\,, \tag{4.1}$$

where the boundary of $\mathcal{D}$ is

$$\partial\mathcal{D} = \{(x, y) : \ I(x, y) - \mathcal{T} = 0\}\,. \tag{4.2}$$

In level set notation, we can describe the exposed region by the function $S(x, y)$:

$$S(x, y) = H(I(x, y; z) - \mathcal{T}) = \begin{cases} S_{int} = 1 & \text{if } \{(x, y) \ : \ I(x, y; z) > \mathcal{T}\} \\ S_{ext} = 0 & \text{if } \{(x, y) \ : \ I(x, y; z) < \mathcal{T}\} \ . \end{cases} \tag{4.3}$$

Under this description, $S(x, y)$ is tied to the image intensity function which is now used as the level set function of the forward problem. By the definition of the exposed region function $S(x, y)$, one can now state an inverse problem to find a desired mask pattern.

In order to achieve our goal, we formulate a least squares problem by defining a cost function

$$C = \iint |T(x, y) - S(x, y)|^2 \, dx \, dy\,, \tag{4.4}$$

where the target mask pattern $T(x, y)$ is given.

Here, we can think of the binary mask function $m(x, y)$ as the desired unknown. Consider a region $\mathcal{M}$ defined by a function $\phi(x, y)$ as follows;

$$\mathcal{M} = \{(x, y) \ : \ \phi(x, y; z) < 0\}\,, \tag{4.5}$$

where the boundary of $\mathcal{M}$ is

$$\partial\mathcal{M} = \{(x, y) : \ \phi(x, y) = 0\}\,. \tag{4.6}$$

Now, in level set notation, we can link this unknown function $\phi(x, y)$ to the desired

mask function $m(x, y)$ by

$$m(x,y) = H(-\phi(x,y)) = \begin{cases} m_{ext} = 0 & \text{if } \{(x,y) \ : \ \phi(x,y) > 0\} \\ m_{int} = 1 & \text{if } \{(x,y) \ : \ \phi(x,y) < 0\} \ . \end{cases} \tag{4.7}$$

Hence $m(x, y)$ is defined by a level set function $\phi(x, y)$ of the inverse problem. We discuss these in detail in Section 4.3.

Now, in order to attack the least squares problem given in Eq. (4.4) we will follow the calculation of variations approach detailed in [35, 36]. This approach will then lead us to a Hamilton-Jacobi equation. However, we first discuss a preliminary on volume and surface integrals of a function f over some region Ω, and some boundary $\partial\Omega$, respectively.

4.2 Preliminary on Volume and Surface Integrals

Here, we follow the preliminary on volume and surface integrals outlined in [37] closely. Let us first define the *characteristic function* χ^- of an interior region Ω^- as

$$\chi^-(\mathbf{x}) = \begin{cases} 1, & \text{if } \phi(\mathbf{x}) \leq 0 \\ 0, & \text{if } \phi(\mathbf{x}) > 0 \, , \end{cases} \tag{4.8}$$

where the boundary is arbitrarily included with the interior region. Here $\mathbf{x} = (x, y)$. The characteristic function χ^+ of an exterior region Ω^+ is defined in a similar way as

$$\chi^+(\mathbf{x}) = \begin{cases} 0, & \text{if } \phi(\mathbf{x}) \leq 0 \\ 1, & \text{if } \phi(\mathbf{x}) > 0 \, , \end{cases} \tag{4.9}$$

again including the boundary with the interior region. For simplicity we restrict ourselves to work with functions of one-dimensional variable ϕ, and use the one-dimensional

Heaviside function

$$H(\phi) = \begin{cases} 0, & \text{if } \phi \leq 0 \\ 1, & \text{if } \phi > 0\,, \end{cases} \tag{4.10}$$

where ϕ depends on $\mathbf{x}$. This allows us to work with H in one spatial dimension. Note that $\chi^+(\mathbf{x}) = H(\phi(\mathbf{x}))$, and $\chi^-(\mathbf{x}) = 1 - H(\phi(\mathbf{x}))$ for all $\mathbf{x}$. The *volume integral* (area or length integral in $\mathbf{R}^2$ or $\mathbf{R}$, respectively) of a function f over interior region Ω^- is then defined as

$$\int_{\Omega} f(\mathbf{x})\chi^-(\mathbf{x})d\mathbf{x}\,. \tag{4.11}$$

Since Ω^- prunes out the exterior region Ω^+ automatically, the region of integration of this integral is all of Ω. One can use the Heaviside function given in Eq. (4.10) to rewrite Eq. (4.11) as

$$\int_{\Omega} f(\mathbf{x})(1 - H(\phi(\mathbf{x}))d\mathbf{x}\,, \tag{4.12}$$

representing the integral of f over the interior region Ω^-. Similarly,

$$\int_{\Omega} f(\mathbf{x})H(\phi(\mathbf{x}))d\mathbf{x}\,, \tag{4.13}$$

is the integral of f over the exterior region Ω^+.

The definition of the Dirac delta function can be given by the directional derivative of the Heaviside function H in the normal direction $\mathbf{N}$ as follows

$$\boldsymbol{\delta}(\mathbf{x}) = \nabla H(\phi(\mathbf{x})) \cdot \mathbf{N}\,, \tag{4.14}$$

which is again a function of variable $\mathbf{x}$. Note that this distribution is nonzero only on the surface $\partial\Omega$ where $\phi = 0$. One can rewrite Eq. (4.14) as

$$\boldsymbol{\delta}(\mathbf{x}) = H'(\phi(\mathbf{x}))\nabla\phi(\mathbf{x}) \cdot \frac{\nabla\phi(\mathbf{x})}{|\nabla\phi(\mathbf{x})|} = H'(\phi(\mathbf{x}))|\nabla\phi(\mathbf{x})|\,, \tag{4.15}$$

using the chain rule and the fact that $\nabla\phi(\mathbf{x}) \cdot \nabla\phi(\mathbf{x}) = |\nabla\phi(\mathbf{x})|^2$. Similarly in one

dimension, the delta function can be defined as the derivative of the one-dimensional Heaviside function

$$\delta(\phi) = H'(\phi), \tag{4.16}$$

where $H(\phi)$ is given by Eq. (4.10). Once again, the delta function $\delta(\phi)$ is identically zero everywhere except at $\phi = 0$. This allows us to rewrite equations (4.14) and (4.15) as

$$\boldsymbol{\delta}(\mathbf{x}) = \delta(\phi(\mathbf{x}))|\nabla\phi(\mathbf{x})|\,, \tag{4.17}$$

using the definition in Eq. (4.16).

The *surface integral* (line or point integral in $\mathbf{R}^2$ or $\mathbf{R}$, respectively) of a function f over the boundary $\partial\Omega$ is defined as

$$\int_{\Omega} f(\mathbf{x})\boldsymbol{\delta}(\mathbf{x})d\mathbf{x}\,, \tag{4.18}$$

where the integration is over all of Ω, since $\boldsymbol{\delta}$ prunes out everything $\partial\Omega$ automatically. One can rewrite this surface integral as

$$\int_{\Omega} f(\mathbf{x})\delta(\phi(\mathbf{x}))|\nabla\phi(\mathbf{x})|d\mathbf{x}\,, \tag{4.19}$$

by using Eq. (4.17). This equation will be used in the derivation of the Hamilton-Jacobi equation in the next section.

4.3 Calculation of Variations

We now use a variational approach to find the mask function $m(x, y)$ that minimizes the cost function C given by Eq. (4.4). Our approach is similar to that of Refs. [35, 36]. We begin by finding the variation of the cost function C, *i.e.*

$$\delta C = -2\iint_{R^2} (T - S)(x, y)\,\delta S\,dx\,dy\,. \tag{4.20}$$

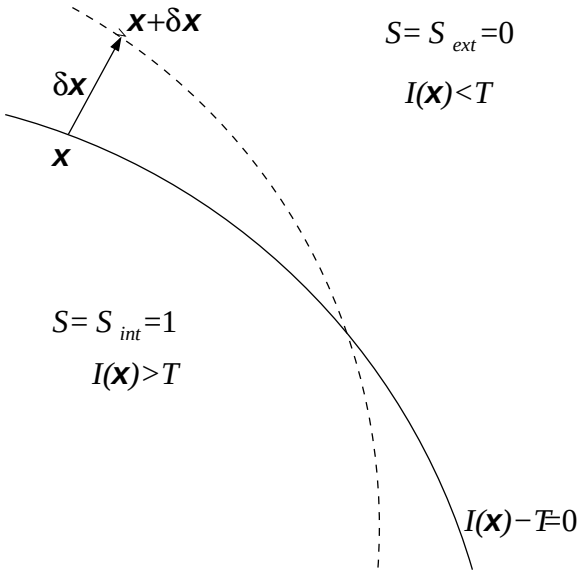

Figure 4.1: The geometry of the variation of the curve $\{(x,y):\ I(x,y)-\mathcal{T}=0\}$ under a variation $\delta I(x,y)$.

Let us now study the geometry of the zero level set $\partial\mathcal{D}$ given in Eq. (4.2) under a variation in $I(x,y)$. Consider the situation depicted in Figure 4.1. The solid curve is the zero level set before $I(\mathbf{x})$ is varied, and the dashed curve is the zero level set of $I+\delta I$. Once again $\mathbf{x}$ denotes $\mathbf{x}=(x,y)$. Suppose the set $\mathcal{D}$ becomes $\mathcal{D}'$ under the variation in $I(\mathbf{x})$. A point $\mathbf{x}$ on the zero level set has been displaced by $\delta\mathbf{x}$. If the variation δS is integrated against a test function $f(\mathbf{x})$ then

$$< \delta S, f >:= \iint\limits_{R^2} \delta S(\mathbf{x})\, f(\mathbf{x}) d\mathbf{x} = \iint\limits_{\text{sym. diff. } (\mathcal{D},\mathcal{D}')} \delta S(\mathbf{x})\, f(\mathbf{x}) d\mathbf{x}\,, \tag{4.21}$$

where sym. diff. $(\mathcal{D},\mathcal{D}') = (\mathcal{D}\cup\mathcal{D}')\setminus(\mathcal{D}\cap\mathcal{D}')$ is the symmetric difference of the sets $\mathcal{D}$ and $\mathcal{D}'$. We can reduce the area integral to a line integral since the difference between $\mathcal{D}$ and $\mathcal{D}'$ is infinitesimal. Let $\mathbf{n}_1 = -\dfrac{\nabla I}{|\nabla I|}$ denote the unit normal along the opposite direction of gradient of intensity. Here, we use the fact that $\delta S(\mathbf{x})$ is either plus or minus $(S_{int}-S_{ext})$; plus when $\delta\mathbf{x}\cdot\mathbf{n_1}(\mathbf{x})$ is negative, and minus otherwise. Hence, the

integral becomes

$$< \delta S, f >:= \int_{\partial \mathcal{D}} (S_{int} - S_{ext})\, \delta \mathbf{x} \cdot \mathbf{n_1}(\mathbf{x})\, f(\mathbf{x}) ds(\mathbf{x})\,, \tag{4.22}$$

where $ds(\mathbf{x})$ is the incremental arclength.

One can now identify that

$$\delta S = (S_{int} - S_{ext})\, \mathbf{n_1} \cdot \delta \mathbf{x} \mid_{\partial D} = \mathbf{n} \cdot \delta \mathbf{x} \mid_{\partial D} = - \frac{\nabla I}{|\nabla I|} \cdot \delta \mathbf{x} \Big|_{\partial D}\,. \tag{4.23}$$

If we then go back to Eq. (4.20), we write

$$\delta C = -2 \iint_{R^2} (T - S)(\mathbf{x})\, \delta S\, d\mathbf{x} = 2 \int_{\partial D} (T - S)(\mathbf{x})\, \frac{\nabla I}{|\nabla I|} \cdot \delta \mathbf{x}\, ds(\mathbf{x})\,. \tag{4.24}$$

In order to remove $\delta \mathbf{x}$, consider the variation of

$$I(\mathbf{x}) - \mathcal{T} = 0\,. \tag{4.25}$$

One can easily show that

$$\nabla I \cdot \delta \mathbf{x} = -\delta I\,. \tag{4.26}$$

By substituting Eq. (4.26) into Eq. (4.24) we obtain

$$\delta C = -2 \int_{\partial D} (T - S)(\mathbf{x})\, \frac{\delta I}{|\nabla I|}\, ds(\mathbf{x})\,. \tag{4.27}$$

Previously we showed in Eq. (3.38) that

$$I(\mathbf{x}) = \sum_n \sigma_n \mid (V_n * m)(\mathbf{x})|^2 = \sum_n \sigma_n \, (V_n * m)\,(\mathbf{x}) (\overline{V}_n * m)(\mathbf{x})\,, \tag{4.28}$$

where $m(\mathbf{x})$ is real valued. The variation of $I(\mathbf{x})$ is then given by

$$\delta I = 2 \sum_n \sigma_n \, \mathrm{Re}\left[(V_n * m)\, (\overline{V}_n * \delta m) \right]\,. \tag{4.29}$$

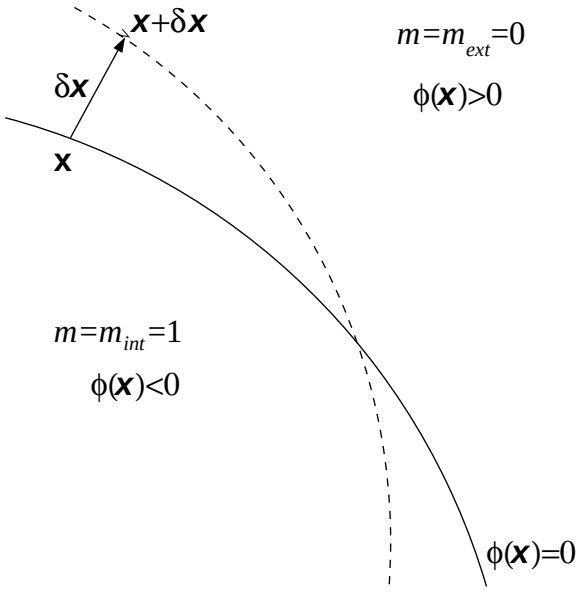

Figure 4.2: The geometry of the variation of the curve $\{(x, y) : \ \phi(x, y) = 0\}$ under a variation $\delta\phi(x, y)$.

Let us now study the geometry of the zero level set $\partial\mathcal{M}$ given in Eq. (4.6) under a variation in $\phi(\mathbf{x})$. Consider the situation depicted in Figure 4.2. The solid curve is the zero level set before ϕ is varied and the dashed curve is the zero level set of $\phi + \delta\phi$. Suppose the set $\mathcal{M}$ becomes $\mathcal{M}'$ under the variation in $\phi(\mathbf{x})$. A point $\mathbf{x}$ on the zero level set has been displaced by $\delta\mathbf{x}$. If the variation δm is integrated against a test function $f(\mathbf{x})$ then

$$< \delta m, f >:= \iint_{R^2} \delta m(\mathbf{x})\, f(\mathbf{x}) d\mathbf{x} = \iint_{\text{sym. diff. } (\mathcal{M},\mathcal{M}')} \delta m(\mathbf{x})\, f(\mathbf{x}) d\mathbf{x}\,, \tag{4.30}$$

where sym. diff. $(\mathcal{M}, \mathcal{M}') = (\mathcal{M} \cup \mathcal{M}') \setminus (\mathcal{M} \cap \mathcal{M}')$ is the symmetric difference of the sets $\mathcal{M}$ and $\mathcal{M}'$. We can now reduce the area integral to a line integral since the difference between $\mathcal{M}$ and $\mathcal{M}'$ is again infinitesimal. Let $\mathbf{n}_2 = \dfrac{\nabla\phi}{|\nabla\phi|}$ denote the unit normal along the direction of gradient of $\phi(\mathbf{x})$. Here, we use the fact that $\delta m(\mathbf{x})$ is either plus or minus $(m_{int} - m_{ext})$; plus when $\delta\mathbf{x} \cdot \mathbf{n_2}(\mathbf{x})$ is positive, and minus otherwise. Hence, the

integral becomes

$$< \delta m, f >:= \int_{\partial \mathcal{M}} (m_{int} - m_{ext})\, \delta \mathbf{x} \cdot \mathbf{n_2}(\mathbf{x})\, f(\mathbf{x}) ds(\mathbf{x})\,, \tag{4.31}$$

where $ds(\mathbf{x})$ is again the incremental arclength.

One can now identify that

$$\delta m = (m_{int} - m_{ext})\, \mathbf{n_2} \cdot \delta \mathbf{x} \mid_{\partial M} = \mathbf{n_2} \cdot \delta \mathbf{x} \mid_{\partial M} = \frac{\nabla \phi}{|\nabla \phi|} \cdot \delta \mathbf{x} \Big|_{\partial M}\,. \tag{4.32}$$

In order to remove $\delta \mathbf{x}$ consider the variation of $\phi(\mathbf{x}) = 0$. We find that

$$\nabla \phi \cdot \delta \mathbf{x} = -\delta \phi\,, \tag{4.33}$$

and therefore obtain

$$\delta m = -\left(\frac{\delta \phi}{|\nabla \phi|} \right) \Big|_{\partial \mathcal{M}}\,. \tag{4.34}$$

By substituting this back into Eq. (4.29) we get

$$\delta I = -2 \sum_n \sigma_n \ \mathrm{Re} \left[(V_n * m)\,(\mathbf{x}) \left(\overline{V}_n * \left(\frac{\delta \phi}{|\nabla \phi|} \right) \Big|_{\partial \mathcal{M}} \right) \right]\,. \tag{4.35}$$

The substitution of Eq. (4.35) into Eq. (4.27) then yields

$$\delta C = 4 \int_{\partial D} \frac{(T-S)(\mathbf{x})}{|\nabla I(\mathbf{x})|} \left\{ \sum_n \sigma_n \ \mathrm{Re} \left[(V_n * m)\,(\mathbf{x}) \left(\overline{V}_n * \left(\frac{\delta \phi}{|\nabla \phi|} \right) \Big|_{\partial \mathcal{M}} \right) \right] \right\} ds\,. \tag{4.36}$$

Since $(T-S)(\mathbf{x})$ is real valued, one can rewrite Eq. (4.36) as

$$\delta C = \sum_n \ \mathrm{Re} \left\{ 4 \int_{\partial D} \frac{(T-S)(\mathbf{x})}{|\nabla I(\mathbf{x})|}\ \sigma_n\ (V_n * m)\,(\mathbf{x}) \left(\overline{V}_n * \left(\frac{\delta \phi}{|\nabla \phi|} \right) \Big|_{\partial \mathcal{M}} \right) \right\} ds\,. \tag{4.37}$$

By re-arranging this integral one gets

$$\delta C = D_\phi C \cdot \delta\phi = \int\limits_{\partial\mathcal{M}} F(\mathbf{x}') \, \frac{\delta\phi(\mathbf{x}')}{|\nabla\phi(\mathbf{x}')|} \, ds(\mathbf{x}') \,, \tag{4.38}$$

where

$$F(\mathbf{x}') \equiv \sum_n \, \mathrm{Re} \int\limits_{R^2} 4(T-S)(\mathbf{x}) \; \sigma_n \; (V_n * m)(\mathbf{x}) \; \overline{V}_n(\mathbf{x}-\mathbf{x}') \; \delta(I(\mathbf{x}) - \mathcal{T}) \, d\mathbf{x} \,, \tag{4.39}$$

where $\delta(I(\mathbf{x}) - t)$ is a Delta function as used in Eq. (4.19). Let us now consider the situation where the surface $\phi(\mathbf{x})$ is altered so that the points on the level curve will move perpendicular to it, that is

$$\delta\phi + v(\mathbf{x}) \, |\nabla\phi| = 0 \,. \tag{4.40}$$

This equation is equivalent to a Hamilton-Jacobi equation (see Section 4.4 for more details) if we view the change as occurring continuously in time [36]. The function $v(x)$ denotes the velocity of the level curves.

Choosing the velocity field is equivalent of choosing a descent direction for the optimization. We choose a steepest descent direction by setting

$$\delta\phi = -F \, |\nabla\phi| \; . \tag{4.41}$$

By substituting $\delta\phi$ given in Eq. (4.41) into Eq. (4.38), we can conclude that it is a descent direction and we can identify the velocity field $v(\mathbf{x})$ as

$$v(\mathbf{x}) = F(\mathbf{x}) \,. \tag{4.42}$$

Here, one must note that we have naturally extended the velocity from its value on the zero level set $\partial\mathcal{M}$ to the entire domain R^2 using the fact that T, S, V_n and m are all defined on R^2. The only requirement for the velocity to correspond to a descent direction is for its value to be specified as F on $\partial\mathcal{M}$ [36].

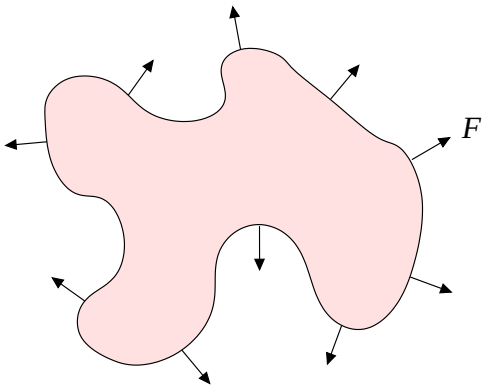

Figure 4.3: An interface evolving with the speed function F.

4.4 The Level Set Method

The level set method was developed by Osher and Sethian [32] for problems involving the motion of curves and surfaces. Consider a closed moving interface $\Gamma(t)$ in $\mathbb{R}^n$. Let $\Omega(t)$ be the region that $\Gamma(t)$ encloses. We associate with $\Omega(t)$ an auxiliary function $\phi(x,t)$, called *the level set function* that is Lipschitz continuous and satisfies the following conditions

$$\begin{cases} \phi(\mathbf{x},t) < 0, & \text{in } \Omega(t); \\ \phi(\mathbf{x},t) = 0, & \text{on } \Gamma(t); \\ \phi(\mathbf{x},t) > 0, & \text{in } \mathbb{R}^n \setminus \overline{\Omega}(t)\,, \end{cases} \tag{4.43}$$

where $\mathbf{x} \in \mathbb{R}^n$ and $t \in \mathbb{R}^+$. The initial condition of the auxiliary function is defined by the signed distance function

$$\phi(\mathbf{x}, t=0) = \pm d(\mathbf{x})\,. \tag{4.44}$$

Here $d(\mathbf{x})$ is the distance from $\mathbf{x}$ to the initial interface $\Gamma(t=0)$, and the sign is determined so that it is negative on the inside of the initial interface, while positive on the outside [38].

The evolution equation for the interface can be written in terms of ϕ. Assume that

$\mathbf{x}(t)$ is a point on the interface that evolves with the interface, then

$$\phi(\mathbf{x}(t), t) = 0\,. \tag{4.45}$$

Differentiating Eq. (4.45) with respect to t gives

$$\phi_t + \nabla\phi(\mathbf{x}, t) \cdot \dot{\mathbf{x}} = 0\,. \tag{4.46}$$

Since F is the speed in the outward normal direction, one can write $\dot{\mathbf{x}} \cdot \mathbf{n} = F$, where $\mathbf{n} = \nabla\phi/|\nabla\phi|$ is the unit normal [39] (See Figure 4.3) . This yields an evolution equation that is an initial value partial differential equation (PDE) for ϕ, namely

$$\begin{aligned} \phi_t + F\,|\nabla\phi| &= 0 \\ \phi(\mathbf{x}, t = 0) \quad &\text{given}\,, \end{aligned} \tag{4.47}$$

which is also known as the level set equation that was introduced in [32]. Through this equation, the motion of the interface $\Gamma(t)$ is captured so that at anytime t,

$$\Gamma(t) = \{\mathbf{x} \mid \phi(\mathbf{x}, t) = 0\}\,. \tag{4.48}$$

The motion of the interface is illustrated in Figure 4.4. With this formulation, the construction of the initial value partial differential equation given in Eq. (4.47) means that the velocity F is now defined for all the level sets, not just the zero level set corresponding the interface itself [3, 39].

One can be more precise by rewriting the level set equation as

$$\phi_t + F_{\text{ext}}\,|\nabla\phi| = 0\,, \tag{4.49}$$

where F_{ext} is some velocity field that equals to the given speed F at the zero level set. In other words,

$$F_{\text{ext}} = F \quad \text{on} \quad \phi = 0\,. \tag{4.50}$$

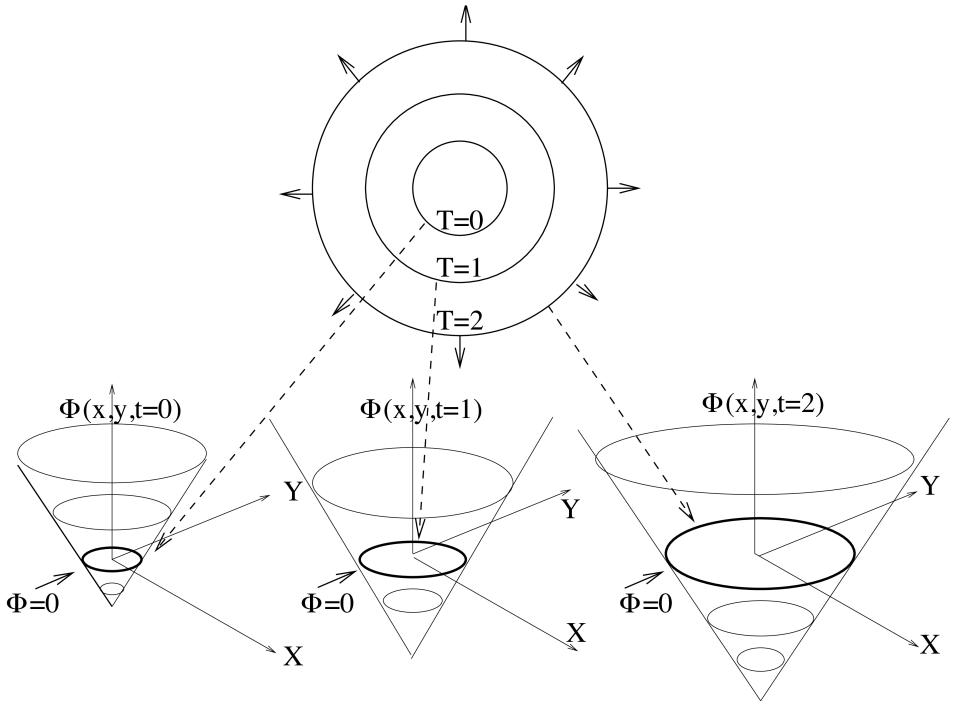

Figure 4.4: Transformation of front motion into initial value problem given in Eq. (4.47) (From [3]).

This implies that the level set method presented in [32] requires the level set function ϕ^n to be updated at every grid point in the computational domain, using a speed function F that has been defined at every point in the computational domain [3]. This new velocity field F_{ext} is known as the *extension velocity.*

4.4.1 Numerical Implementation of The Level Set Method

One important aspect of the paper by Osher and Sethian [32] was the use of the methods borrowed from hyperbolic conservation laws for discretizing the level set equation (4.47). This concept was generalized in [40], where numerical flux functions designed for hyperbolic conservation laws were used to solve *Hamilton-Jacobi equations* of the

form

$$\phi_t + H(\nabla\phi) = 0\,. \tag{4.51}$$

Here, the function $H(\nabla\phi)$ is called *the Hamiltonian*, and it is a function of the gradient of ϕ [39].

In the case of the level set method, the Hamiltonian is given by

$$H(\nabla\phi) = F\,|\nabla\phi|\,. \tag{4.52}$$

Viscosity Solutions of Hamilton-Jacobi Equations

One can rewrite Eq. (4.47) as

$$\phi_t + F\left(\phi_x^2 + \phi_y^2\right)^{1/2} = 0\,, \tag{4.53}$$

in two dimensions. By letting $u = \phi_x$ and $v = \phi_y$, and by differentiating both sides with respect to x and y, one gets a pair of equations for u and v. We cannot simply take the theory of viscous solutions and entropy conditions for hyperbolic conservation laws and integrate this equation upwards. Instead, a better approach would be to work directly with the level set equation, and add a viscosity term to the right-hand side.

More generally, consider the following Hamilton-Jacobi equation,

$$u_t + H(Du, \mathbf{x}) = 0\,, \tag{4.54}$$

where Du represents the partials of u in each variable. Assume that the Hamiltonian H is a smooth function of its arguments. We want to admit non-smooth solutions, that is, those that allow corners. We do this by adding a viscosity term to Eq. (4.54), that is,

$$u_t + H(Du, \mathbf{x}) = \epsilon\Delta u\,, \tag{4.55}$$

where ϵ is a positive constant. Given a solution u_ϵ, one would ideally want to show that such solution is smooth, and that its limit as ϵ goes to zero gives an appropriate weak solution. However, instead of defining the weak solution as a limit of smooth solutions,

one can follow the approach of Refs. [3, 41, 42], and define a weak solution as follows

Definition: u is said to be a viscosity solution of Eq. (4.54), if for all smooth test functions v,

1. if $u - v$ has a local maximum at a point (x_0, t_0) then

$$v_t(x_0, t_0) + H(Dv(x_0, t_0), x_0) \leq 0\,, \tag{4.56}$$

2. if $u - v$ has a local minimum at a point (x_0, t_0) then

$$v_t(x_0, t_0) + H(Dv(x_0, t_0), x_0) \geq 0\,. \tag{4.57}$$

Note that, first, the definition does not differentiate u, but v, and second, it follows the trick of integration by parts, and passes all the derivatives off of u onto v. This turns out to be a reasonable and valuable definition of the solution, since one can show the following [41]:

- If u is a smooth solution of the Hamilton-Jacobi equation, then it is a viscosity solution. In other words, any classical solution that stays smooth for all time satisfies the two inequalities in the definition above.
- If a viscosity solution u is differentiable at some point, then it satisfies the Hamilton-Jacobi equation there. That is to say, where the viscosity solution is smooth, it gives the same answer as the classical solution.
- Given the appropriate initial conditions the above viscosity solution is unique.
- The solution produced by taking the limit of the smooth solutions u_ϵ as ϵ tends to zero is a viscosity solution; by uniqueness, this solution must be one given above.

The reader is referred to [42, 43, 44] for the precise statements and proofs. The scheme we will discuss in the next section is an approximation to the level set equation that has a convex Hamiltonian H. A number of studies have been done to show that this scheme

along with others converge to above viscosity solution [41]. For example, Crandall and Lions analyze an explicit finite difference scheme in [42].

Numerical Approximation of the Level Set Equations

Entropy-satisfying upwind viscosity scheme for initial value formation was introduced by Osher and Sethian [32], leading to the numerical method known as the *level set method*. Following their approach, we use the following first order finite difference approximation to solve Eq. (4.47)

$$\phi_{i\,j\,k}^{n+1} = \phi_{i\,j\,k}^{n} - \Delta t \left(\max(F,0)\, \nabla_{i\,j\,k}^{+} + \min(F,0)\, \nabla_{i\,j\,k}^{-} \right) , \tag{4.58}$$

where

$$\nabla_{i\,j\,k}^{+} = \left[\begin{array}{l} \max\left(D^{-x}\phi_{i\,j\,k}^{n},0\right)^2 + \min\left(D^{+x}\phi_{i\,j\,k}^{n},0\right)^2 + \\ \max\left(D^{-y}\phi_{i\,j\,k}^{n},0\right)^2 + \min\left(D^{+y}\phi_{i\,j\,k}^{n},0\right)^2 + \\ \max\left(D^{-z}\phi_{i\,j\,k}^{n},0\right)^2 + \min\left(D^{+z}\phi_{i\,j\,k}^{n},0\right)^2 \end{array} \right]^{1/2} , \tag{4.59}$$

and

$$\nabla_{i\,j\,k}^{-} = \left[\begin{array}{l} \min\left(D^{-x}\phi_{i\,j\,k}^{n},0\right)^2 + \max\left(D^{+x}\phi_{i\,j\,k}^{n},0\right)^2 + \\ \min\left(D^{-y}\phi_{i\,j\,k}^{n},0\right)^2 + \max\left(D^{+y}\phi_{i\,j\,k}^{n},0\right)^2 + \\ \min\left(D^{-z}\phi_{i\,j\,k}^{n},0\right)^2 + \max\left(D^{+z}\phi_{i\,j\,k}^{n},0\right)^2 \end{array} \right]^{1/2} , \tag{4.60}$$

for a convex speed function F [3, 41]. Here, D^{+x} denotes the forward difference operator in the x-direction,

$$D^{+x}\phi_{i\,j\,k}^{n},0 = \frac{\phi_{i,j,k}^{n} - \phi_{i-1,j,k}^{n}}{\Delta x} , \tag{4.61}$$

whereas D^{-x} denotes the backward difference operator,

$$D^{-x}\phi_{i\,j\,k}^{n},0 = \frac{\phi_{i+1,j,k}^{n} - \phi_{i,j,k}^{n}}{\Delta x} . \tag{4.62}$$

Eq. (4.58) is an explicit scheme and hence can be solved directly. The time step requirement depends on the nature of the speed function F. For an F that depends only on the position, time step behaves like $\dfrac{\Delta t}{\Delta x} F \leq 1$, [3]. This is also known as the

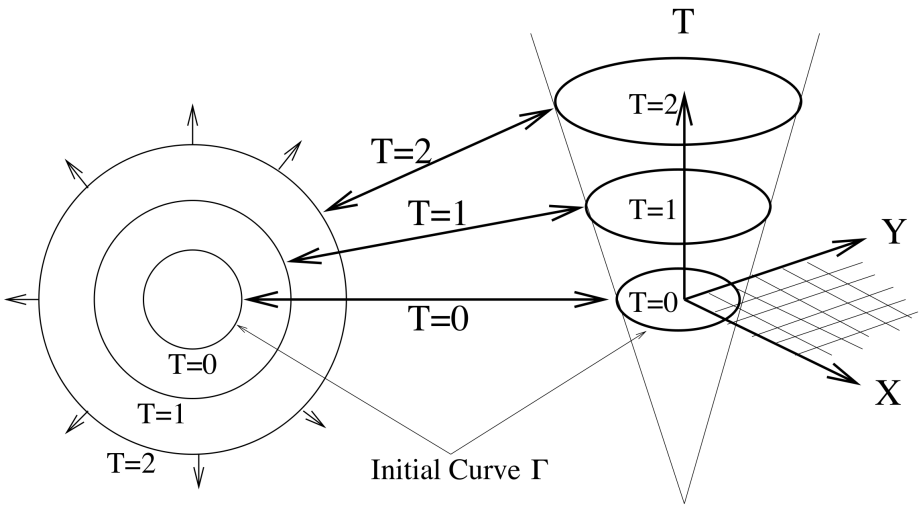

Figure 4.5: Transformation of front motion into boundary value problem given in Eq. (4.65) (From [3])

Courant-Friedrichs-Lewy (CFL) condition .

4.4.2 Initialization with the Fast Marching Method

The Fast Marching Method (FMM) was introduced and developed by Sethian in [34] for solving the problem of front propagation efficiently. Imagine a closed curve Γ in the plane propagating normal to itself with speed F. One way to characterize the position of this expanding front is to compute the arrival time $T(\mathbf{x})$ of the front as it crosses each point (x, y) as shown in Figure 4.5.

Using "time $\times$ velocity = distance", one gets

$$dT \cdot F = dx\,, \tag{4.63}$$

and hence

$$\frac{dT}{dx} F = 1\,. \tag{4.64}$$

More generally, the spatial derivative becomes the gradient, hence we have

$$|\nabla T|\, F = 1, \quad T = 0 \text{ on } \Gamma\,. \tag{4.65}$$

This boundary value problem is also known as the Eikonal equation [3]. This time we discretize Eq. (4.65) with a slightly different upwind scheme than the one we used for the level set equation that was given in Eq. (4.58), *i.e.*,

$$\left[\begin{array}{l} \max\left(D_{ijk}^{-x}T, -D_{ijk}^{+x}T, 0\right)^2 + \\ \max\left(D_{ijk}^{-y}T, -D_{ijk}^{+y}T, 0\right)^2 + \\ \max\left(D_{ijk}^{-z}T, -D_{ijk}^{+z}T, 0\right)^2 \end{array}\right]^{1/2} = \frac{1}{F_{ijk}}\,. \tag{4.66}$$

The forward and backward operators D^{-y}, D^{+y}, D^{-z} and D^{+z} in the coordinate directions are similar to the one defined earlier for the x direction.

The central idea behind the FMM is to systematically construct the solution in a "downwind" fashion. The upwind difference structure of Eq. (4.66) means that information propagates one way, that is, from smaller values of T to larger values (See Figure 4.6). Hence, the algorithm rests on solving Eq. (4.66) by building the solution outward from the smallest T value [3, 45].

Algorithm for The Fast Marching Method

The algorithm proceeds as follows: First, we tag points in the initial conditions as "Accepted", we then tag all points one grid point away as "Close", and finally, we denote all other grid points as "Far". The inner loop therefore consists of the following operations [3],

1. Begin loop: Let *Trial* be the point in *Close* with the smallest value for T.
2. Add the point *Trial* to *Accepted*; remove it from *Close*.
3. Tag as *Close* all neighbors of *Trial* that are not *Accepted*. If the neighbor is in *Far*, remove it from that list and add it to the set *Close*.

4. Recompute the values of T at all neighbors according to Eq. (4.66) by solving and selecting the largest possible solution to the quadratic equation.

5. Return to the top of the loop.

Consider a two dimensional Eikonal equation, in which the boundary value is known at the origin, see Figure 4.6(a). The black sphere at $T_{0,0}$ stands for a grid point where the value of T is known, and the light grey spheres show the grid points where the solution is unknown. We start the algorithm by marching "downwind" from the known value and computing new values at each of the four neighboring grid points as shown in Figure 4.6(a) and Figure 4.6(b). This provides possible values for T at each grid point $T_{-1,0}$, $T_{1,0}$, $T_{0,-1}$, $T_{0,1}$ that are shown in Figure 4.6(b). We now choose the dark grey sphere with the smallest value (for example A in Figure 4.6(c)), and march downwind again from this point as shown by the arrows in Figure 4.6(c). Because of upwinding, no point can be affected by grid points containing larger values of T. Hence, we may freeze the value of T at this smallest dark grey sphere A, and turn it into a black sphere to consider its value known, see Figure 4.6(d). We may then proceed ahead with the algorithm as shown in Figure 4.6(e) and 4.6(f).

This algorithm works because the process of recomputing the T values at upwind neighboring points cannot yield a value smaller than any of the *Accepted* points. This is known as the "monotone property" and means that we can march the solution outward, always selecting the narrow band grid point with minimum trial value for T , and readjusting the neighbors, without having to go back and correct an *Accepted* value. For a rectangular mesh with N grid points, this algorithm scales with the mesh size N as $\mathcal{O}(N \log N)$[3]. We also use periodic boundary conditions.

4.5 Numerical Procedure

In this section we discuss numerical results obtained by using the level set method described above for the solution of Eq. (4.47). First, the aerial intensity image is calculated using Eq. (3.38) for each target mask pattern. Note that the eigenvalues and

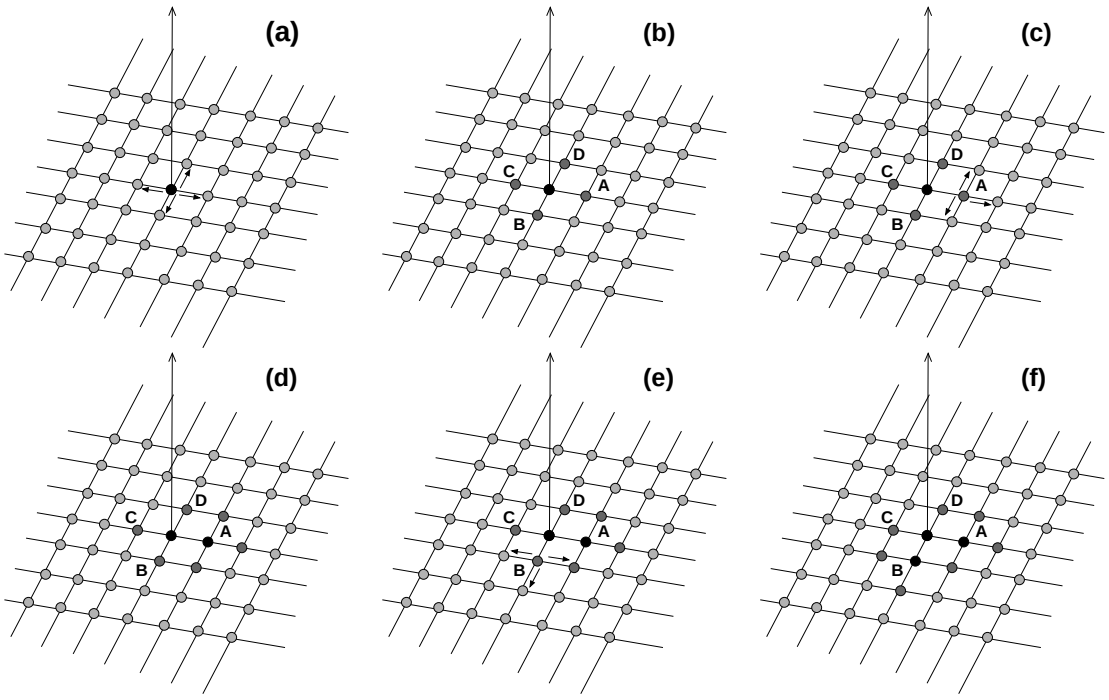

Figure 4.6: (a) Update downwind, (b) Compute new possible values for neighboring points (c) Choose the smallest value (for example A), (d) Freeze value at A, update neighboring points (e) Choose the smallest value (for example B), (f)Freeze value at B, update neighboring points. Continue until all grid points are frozen.

eigenfunctions necessary for this calculation are only computed once for a given set of system specific parameters, and is independent of the mask. The FMM is then used to compute the initial ϕ values from a target pattern layout T. By using this initial value, the level set method (using Eq. (4.58)) yields an exposed pattern S and the output mask layout m that would produce it. We monitor the convergence of the algorithm during the iterations using an error defined as

$$Error = \frac{\text{Number of pixel error}}{N^2} \tag{4.67}$$

where N^2 is the grid size. Here, the "number of pixel error" refers to the number of pixels in S that deviate from the desired target pattern T. Results in this section are

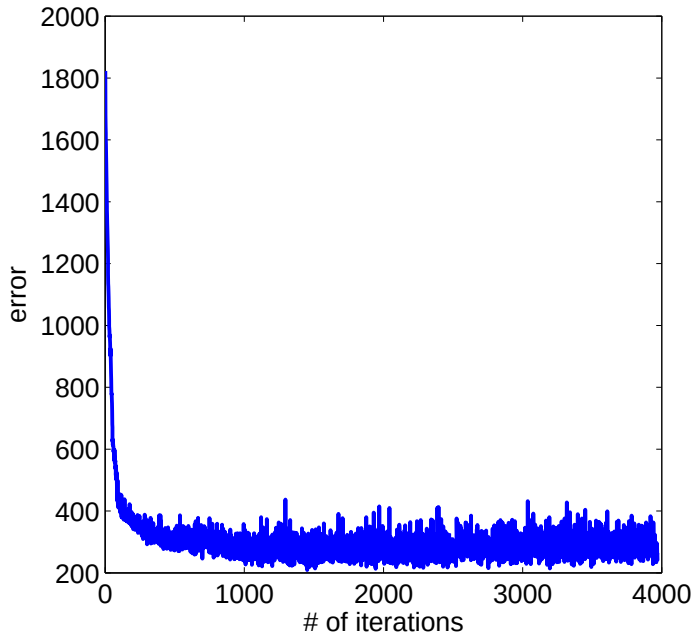

Figure 4.7: A sample error data plot for $N = 128$.

shown for the minimum error that the scheme has reached. A typical error plot is shown in Figure 4.7. As seen in this figure the error rapidly decreases until it starts to oscillate and a base level is reached.

The results are obtained either for $N = 128$ or for $N = 256$. For $N = 128$, each pixel has a length of $\Delta x = 12.5\ nm$, and for $N = 256$ the pixel length is $\Delta x = 6.25\ nm$. Since this is a pixel length and width, Δx and Δy are always taken to be equal to each other. We used a wavelength of $\lambda = 193\ nm$, numerical aperture value of $NA = 0.85$, partial coherence factor of $s = 0.5$.

We start by analyzing the mask pattern, shown in Figure 4.8(a) that has features with width of 6 pixels for $N = 128$, namely 75 nm. The features are 14 pixels apart from each other. For $N = 128$, Figure 4.8(b) shows the mask found as the numerical solution of the inverse problem with 0.09% error. If we take the threshold for exposing the substrate to be of 40% of the intensity, then the resulting exposed pattern is shown in

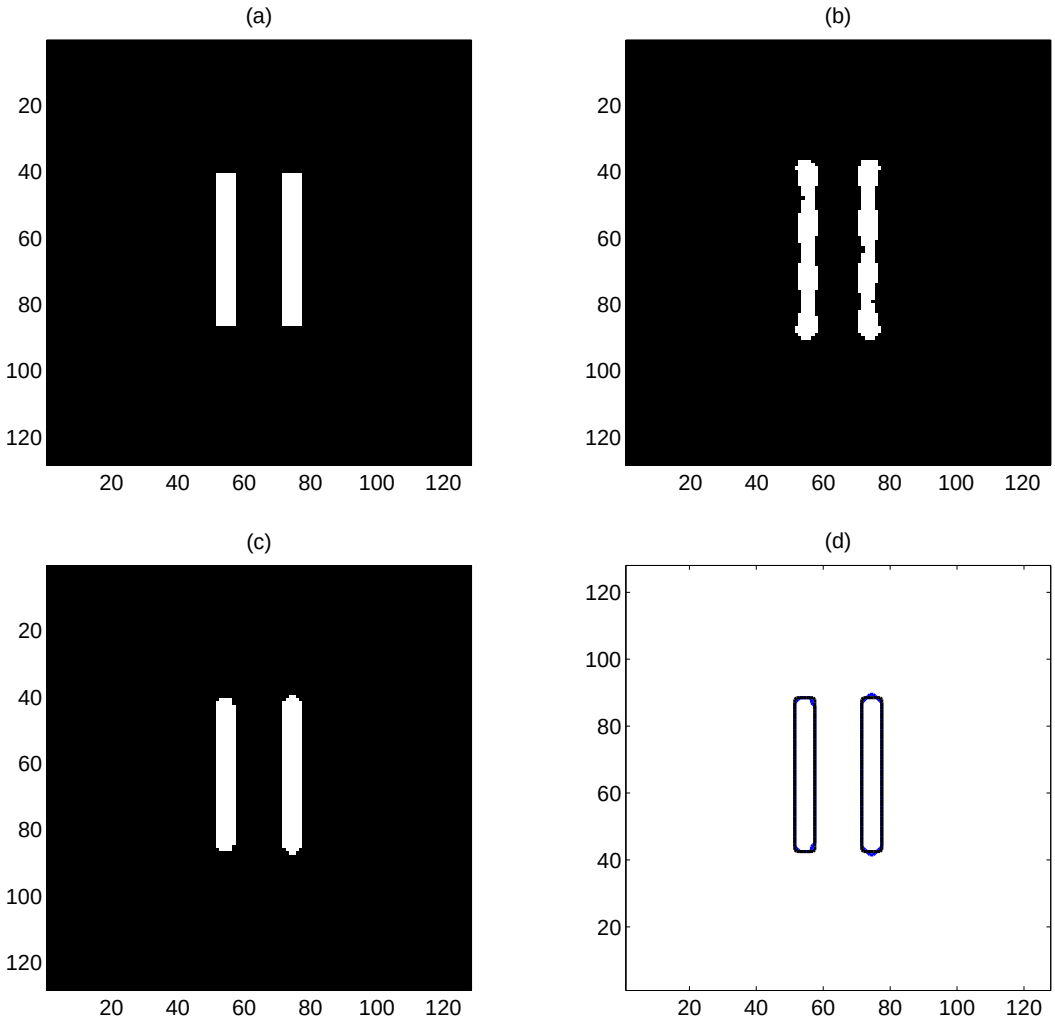

Figure 4.8: (a) Target mask, (b) outcome mask (c) exposed region for 40% (d) contour plot of target mask and the exposed region (exposed region is shown in dark blue color) for $N = 128$, $z = 0$, and 0.09% error.

Figure 4.8(c). For better comparison, the contour plots of target mask and the exposed region are plotted in Figure 4.8(d). The exposed region shows slightly rounded corners as expected in Figure 4.8(d), otherwise does an excellent job producing the desired target mask.

We then analyze the mask pattern shown in Figure 4.9(a) that have features with

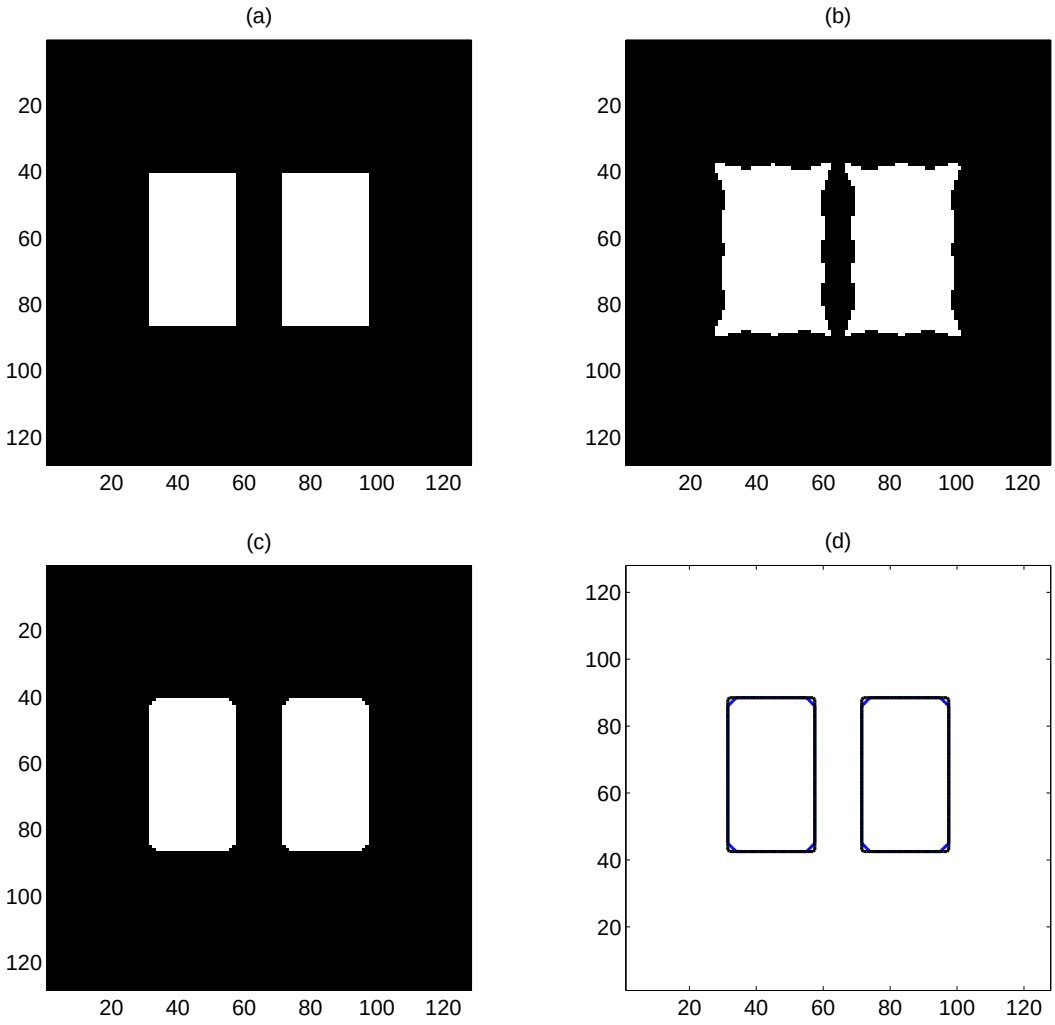

Figure 4.9: (a) Target mask, (b) outcome mask, (c) exposed region for 40%, (d) contour plot of target mask and the exposed region (exposed region is shown in dark blue color) for $N = 128$, $z = 0$, and 0.15% error.

width of 26 pixels. These features are again 14 pixels apart from each other. We used this mask layout to compare the results that are shown in Figure 4.8. The outcome mask is shown in 4.9(b) for $N = 128$ with 0.15% error. The 40% exposed region, shown in Figure 4.9(c), is almost in perfect agreement with the target pattern as shown in Figure 4.9(d). The exposed region has corners that are more square looking.

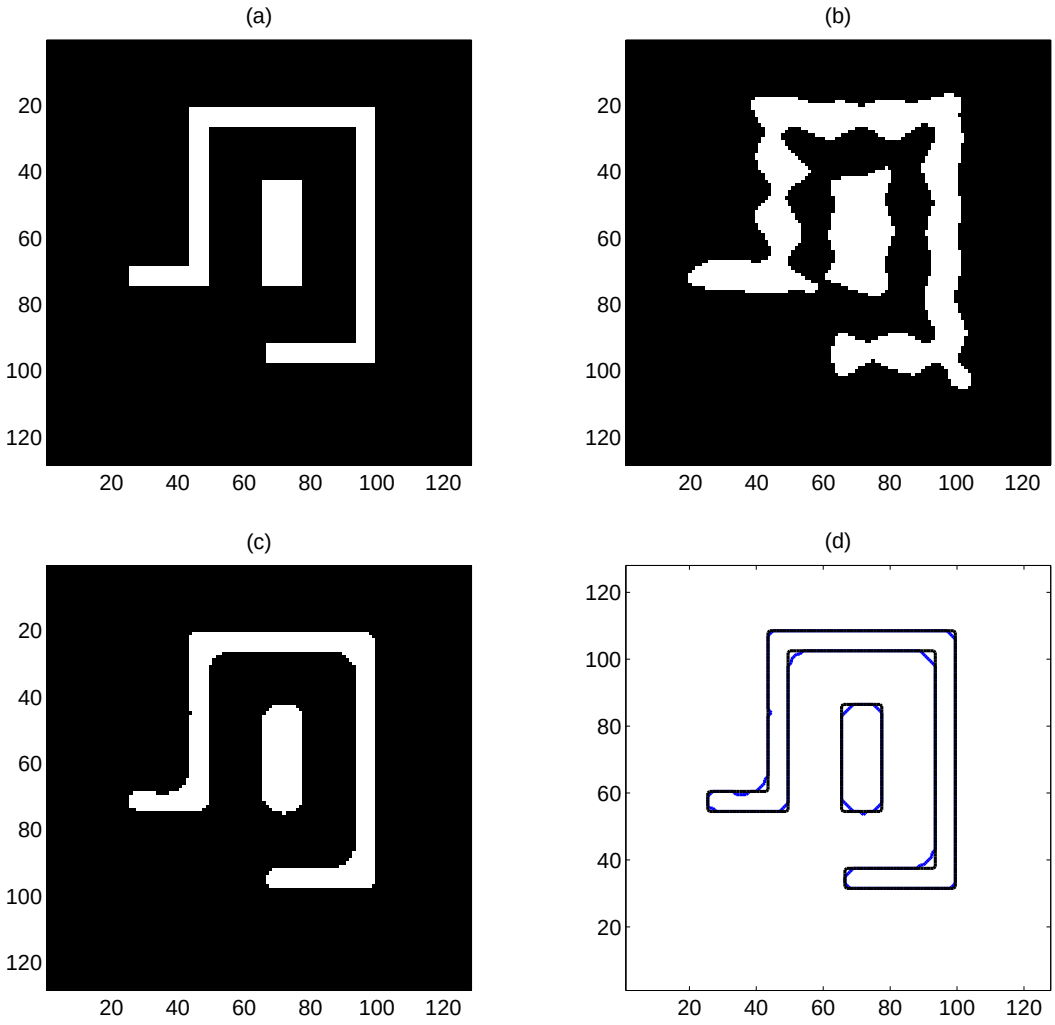

Figure 4.10: (a) Target mask, (b) outcome mask, (c) exposed region for 40%, (d) contour plot of target mask and the exposed region (exposed region is shown in dark blue color) for $N = 128$, $z = 0$, and 0.4% error.

In Figure 4.10(a) we show a mask that has features with width of 6 pixels and a rectangle feature in the middle, with a width of 11 pixels. These features are 14 pixels apart from each other. We used this mask layout to compare with results that are shown in Figure 1.3(b) (the same mask used by Cobb [2]). The outcome mask is shown in 4.10(b) for $N = 128$ with 0.4% error. Note that here $z = 0$. The 40% exposed region,

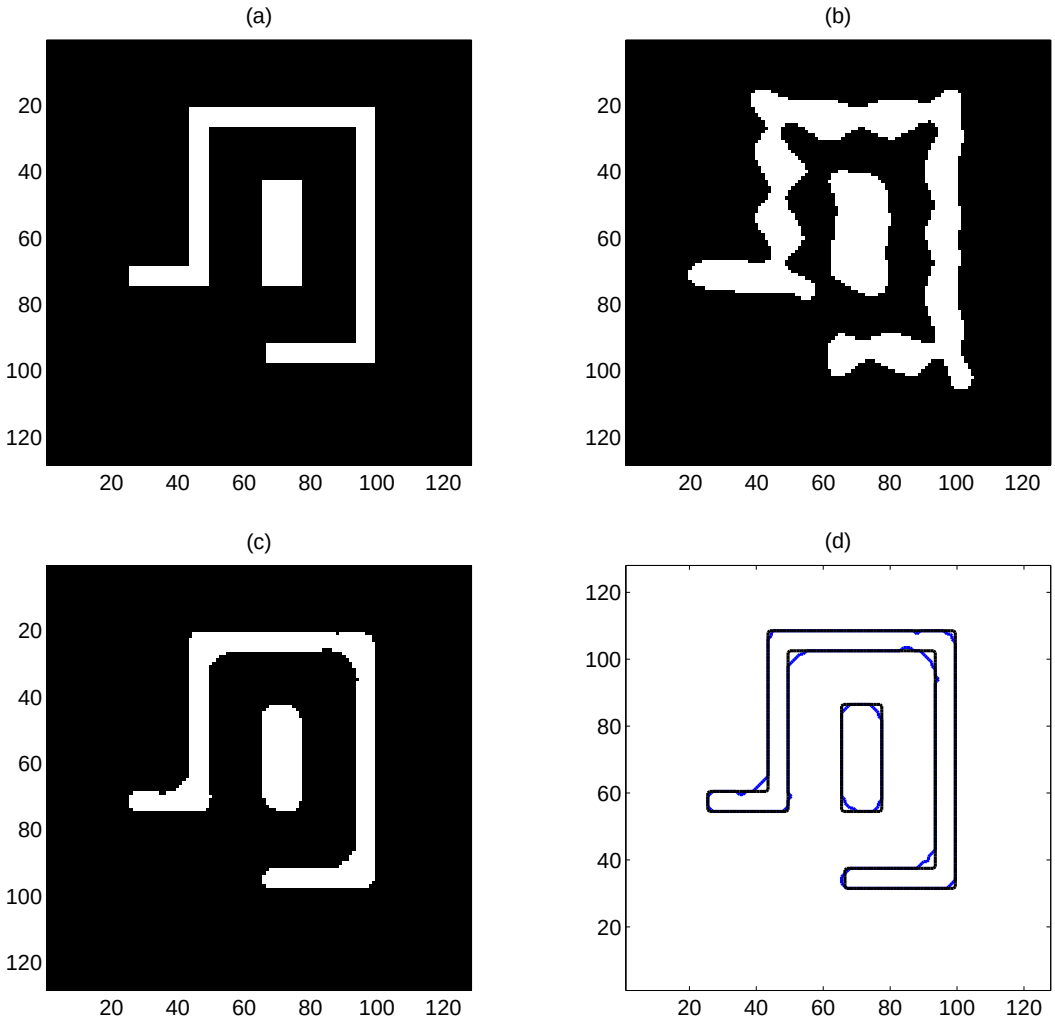

Figure 4.11: (a) Target mask, (b) outcome mask, (c) exposed region for 40%, (d) contour plot of target mask and the exposed region (exposed region is shown in dark blue color) for $N = 128$, $z = 60\ nm$, and 0.6% error.

shown in Figure 4.10(c) and (d), is almost in perfect agreement with the one shown in Figure 1.3. A more detailed comparison shows that our exposed pattern has more square looking corners, and thus would enable better accuracy in manufacturing.

In Figure 4.11(a) we used the same target mask shown in Figure 4.10(a), however the results are shown for $z = 60\ nm$, which represent a more realistic optical system.

The outcome mask is shown in 4.11(b) for $N = 128$ with 0.6% error. Then 40% of the intensity that is exposed by using this outcome mask is shown in Figure 4.11(c). The contour plots of target mask and the exposed region are once again plotted in Figure 4.11(d) for comparison. The exposed region is again in perfect agreement with the one shown in Figure 1.3(b). The change in z does not seem to affect the results for the exposed region dramatically.

In the mask pattern shown in Figure 4.12(a), most of the features have a width of 6 pixels, and they are mostly 6 pixels apart from each other for $N = 128$. Here we again take $z = 0$. In Figure 4.12(b), the outcome mask we were able to produce with 1.4% error does not pick up all the features. The intensity that is exposed by using this outcome mask (again at 40%) is shown in Figure 4.12(c). The contour plots of target mask and the exposed region are then plotted in Figure 4.12(d). Next we increase the width of the feature that did not show up in the outcome mask to 8 pixels as shown in Figure 4.13(a). The outcome mask is shown in Figure 4.12(b) for $N = 128$ obtained with 1.4% error. This mask is able to pick up all the features. The 40% exposed region, shown in Figure 4.13(c), is mostly in good agreement with the target pattern as shown in Figure 4.13(d).

We now present results for the same target mask patterns for $N = 256$. Each mask pattern that was for $N = 128$ is now scaled to $N = 256$. In Figure 4.14(b) the desired outcome mask looks more symmetric, and the features in the exposed region for 40% of intensity is shown Figure 4.8(c) and (d). Here the error is 1.4%. In Figure 4.15(a) the target mask pattern is shown for $N = 256$. These features are 28 pixels apart from each other. We again used this mask layout to compare the results that are shown in Figure 4.14. The outcome mask is shown in 4.15(b) with 0.4% error. The 40% exposed region, shown in Figure 4.15(c), is almost in perfect agreement with the target pattern as shown in Figure 4.15(d). In Figure 4.16(a) we show the target mask pattern that we used to compare results of Figure 1.3(b) for $N = 256$. The outcome mask is shown in 4.16(b) with 0.7% error. Note that here $z = 0$. The 40% exposed region, shown in Figure 4.16(c) and (d), is again in good agreement with the one shown in Figure 1.3(b). Our result shows more square looking corners in the exposed region compared to the

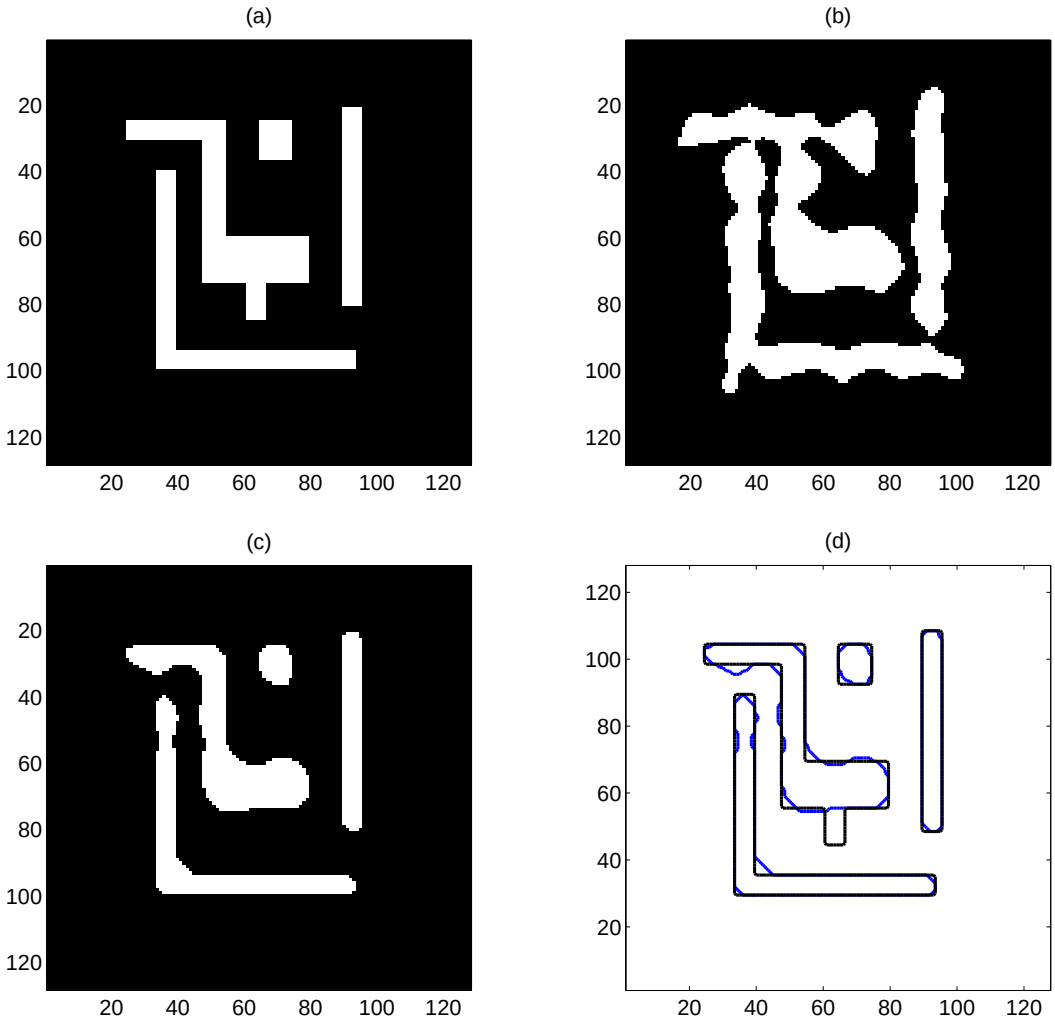

Figure 4.12: (a) Target mask, (b) outcome mask, (c) exposed region for 40%, (d) contour plot of target mask and the exposed region (exposed region is shown in dark blue color) for $N = 128$, $z = 0$, and 1.4% error.

result of $N = 128$ (Figure 4.10(d)).

In Figure 4.17(a) the same target mask shown in Figure 4.16(a) is used. However, the distance z is taken to be 60 nm. The outcome mask is shown in 4.17(b) for $N = 256$ with 0.7% error. The exposed intensity by using this outcome mask is shown in Figure 4.17(c). For comparison, the contour plots of target mask and the exposed region are

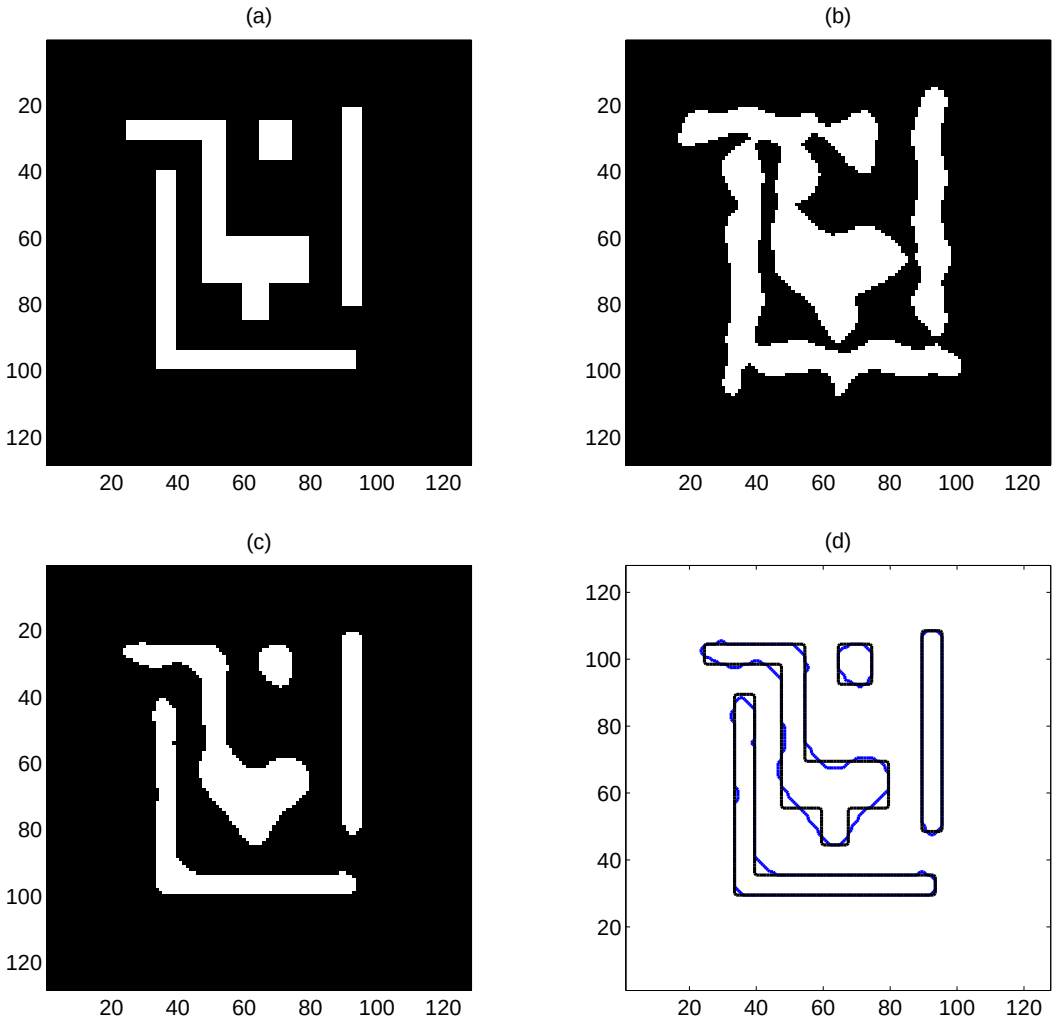

Figure 4.13: (a) Target mask, (b) outcome mask, (c) exposed region for 40%, (d) contour plot of target mask and the exposed region (exposed region is shown in dark blue color) for $N = 128$, $z = 0$, and 1.4% error.

once again plotted in Figure 4.17(d). The exposed region is again in perfect agreement with the one shown in Figure 1.3(b). Similar to case for $N = 128$, the change in z does not seem to make a dramatic change in the results for the exposed region. In the mask pattern shown in Figure 4.18(a) most of the features have a width of 12 pixels and they are mostly 12 pixels apart from each other. The linear size of the mask is $N = 256$. In

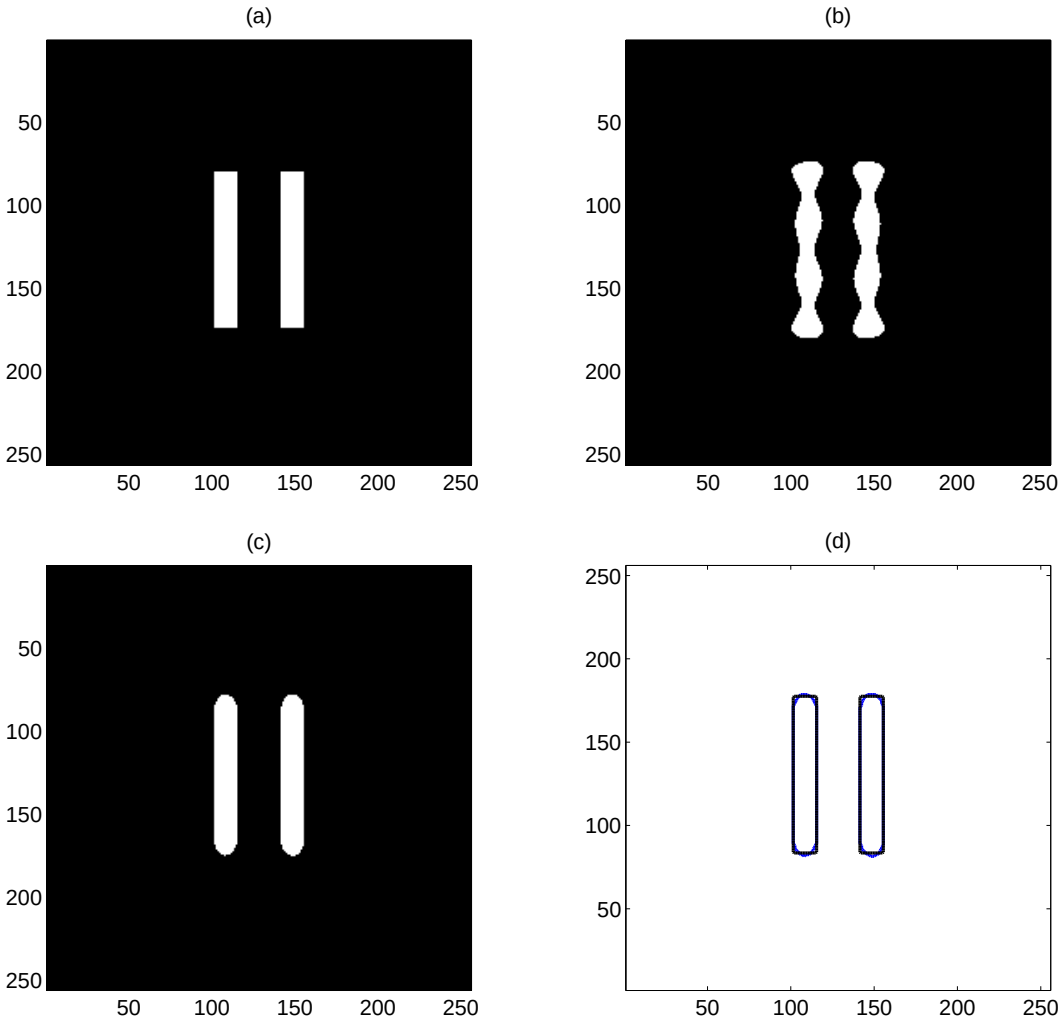

Figure 4.14: (a) Target mask, (b) outcome mask, (c) exposed region for 40%, (d) contour plot of target mask and the exposed region (exposed region is shown in dark blue color) for $N = 256$, $z = 0$, and 1.4% error.

Figure 4.18(b), the outcome mask, produced with 1.6% error for $z = 0$, once more does not pick up all the features. Furthermore the mask seems to be not manufacturable since some of the features are conjoined. Then 40% of the intensity that is exposed by using this outcome mask is shown in Figure 4.18(c). The contour plots of target mask and the exposed region are then plotted in Figure 4.18(d).

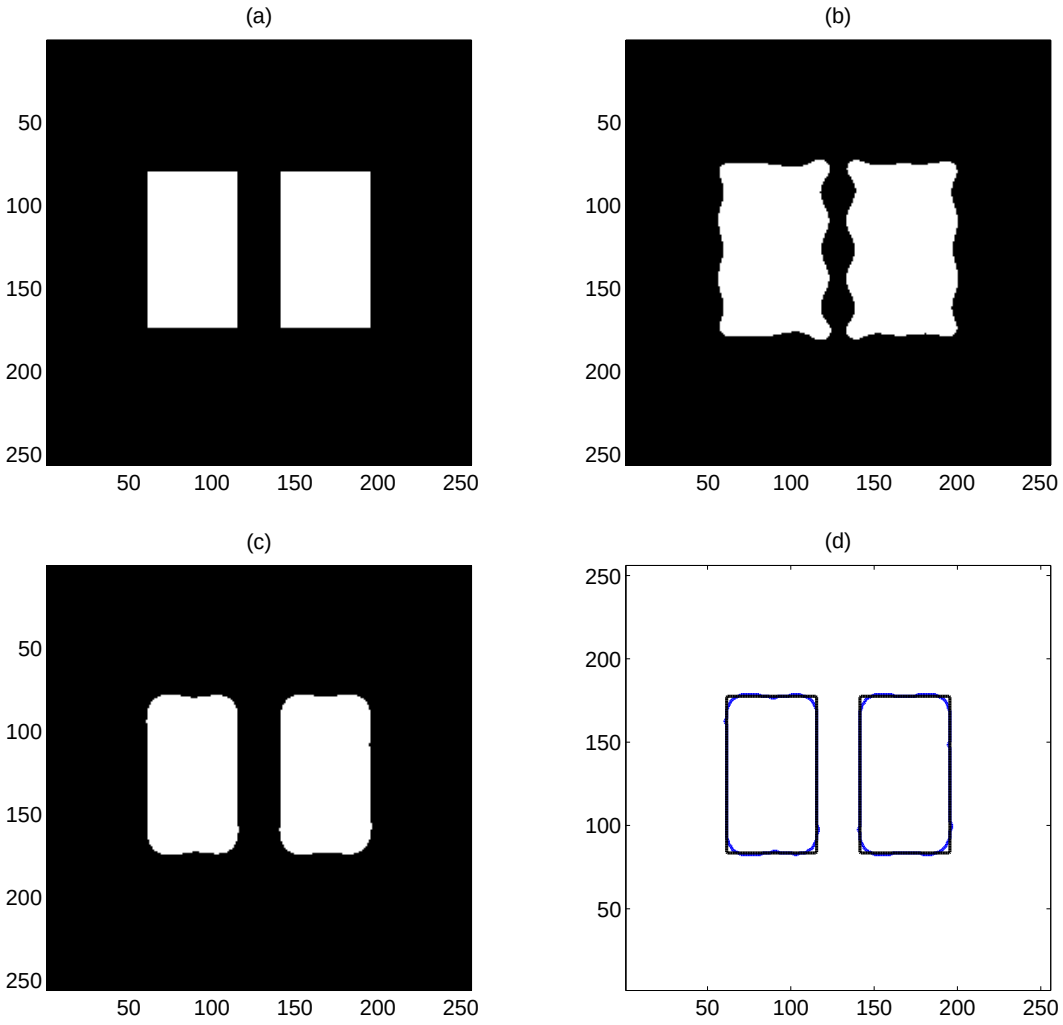

Figure 4.15: (a) Target mask, (b) outcome mask, (c) exposed region for 40%, (d) contour plot of target mask and the exposed region (exposed region is shown in dark blue color) for $N = 256$, $z = 0$, and 0.4% error.

Finally, we use a mask that has an increased width of 16 pixels for the feature that did not show up in the previous mask (see Figure 4.19(a)). The resulting outcome mask is shown in Figure 4.19(b) for $N = 256$ with 1.4% error. Again this mask does not look manufacturable, however it once more picks up all the features. The 40% exposed region, shown in Figure 4.19(c), is mostly in good agreement with the target mask

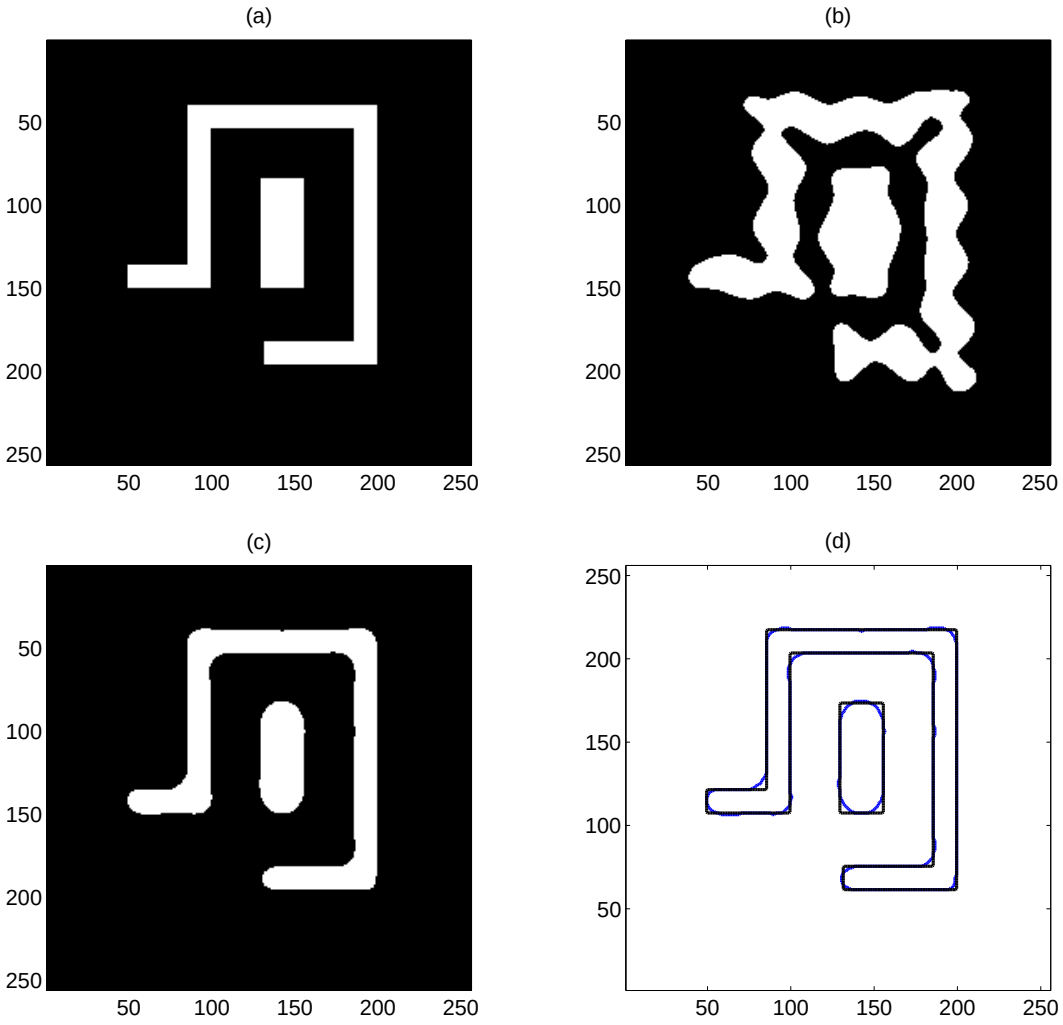

Figure 4.16: (a) Target mask, (b) outcome mask, (c) exposed region for 40%, (d) contour plot of target mask and the exposed region (exposed region is shown in dark blue color) for $N = 256$, $z = 0$, and 0.7% error.

pattern shown in Figure 4.19(d).

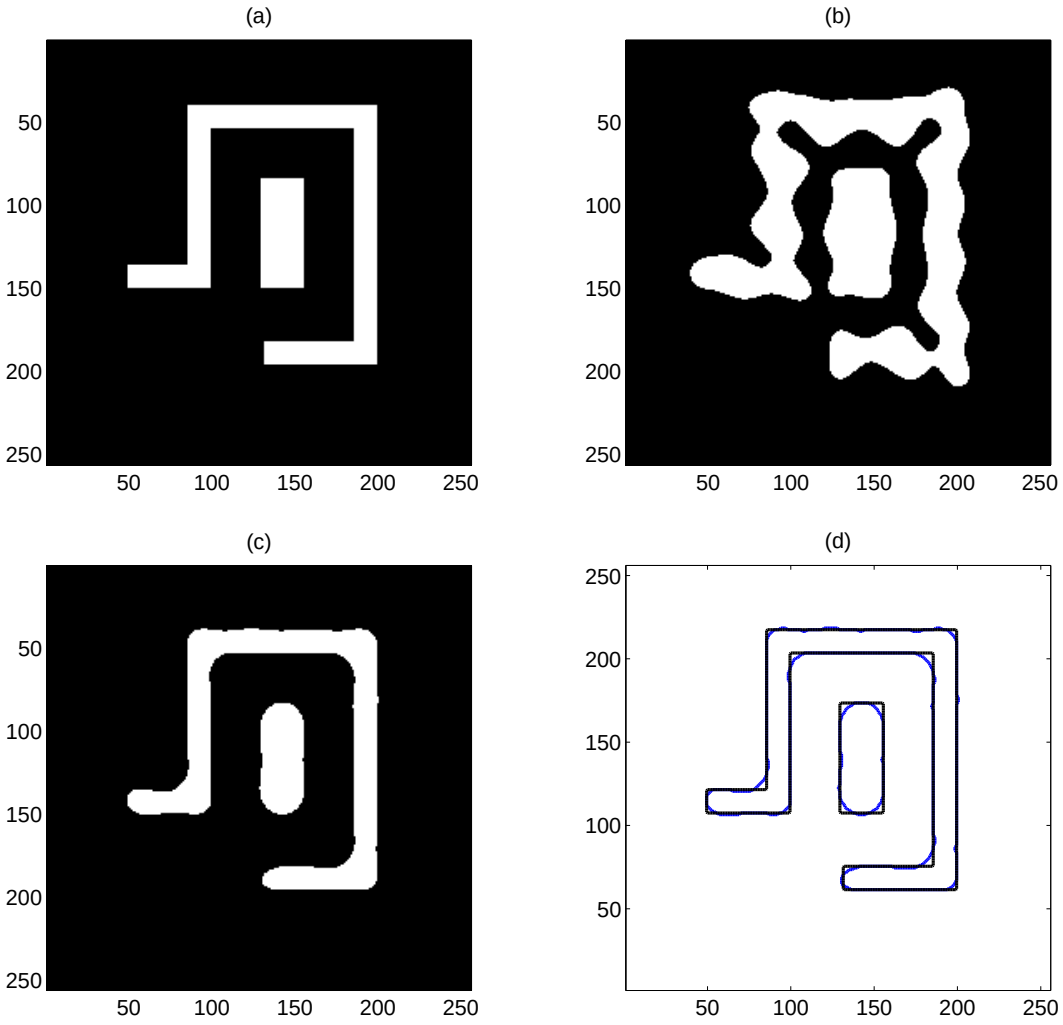

Figure 4.17: (a) Target mask, (b) outcome mask, (c) exposed region for 40%, (d) contour plot of target mask and the exposed region (exposed region is shown in dark blue color) for $N = 256$, $z = 60\ nm$, and 0.7% error.

4.6 Summary

In this chapter, we discussed the level set method for the inverse lithography problem. We defined a cost function, and using the calculus of variations we derived a particular Hamilton-Jacobi equation for the system, that is also known as the level set equation.

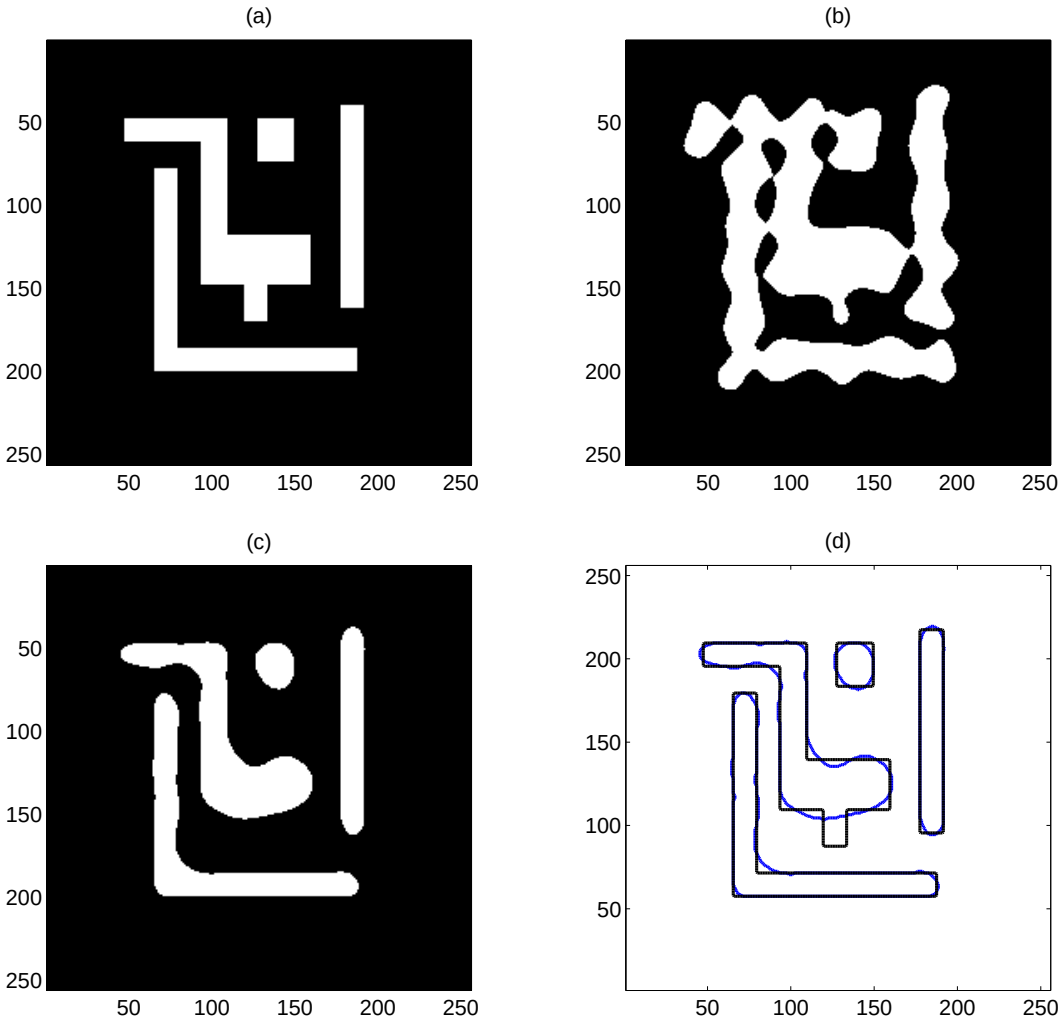

Figure 4.18: (a) Target mask, (b) outcome mask, (c) exposed region for 40%, (d) contour plot of target mask and the exposed region (exposed region is shown in dark blue color) for $N = 256$, $z = 0$, and 1.6% error.

We then discussed the implementation of the level set method and the fast marching method used to generate the initial surface. We then presented our numerical results obtained using different mask patterns.

Our results showed excellent agreement with the earlier work of Cobb [2]. In fact, our approach was able to capture the sharp corners in their mask much more accurately.

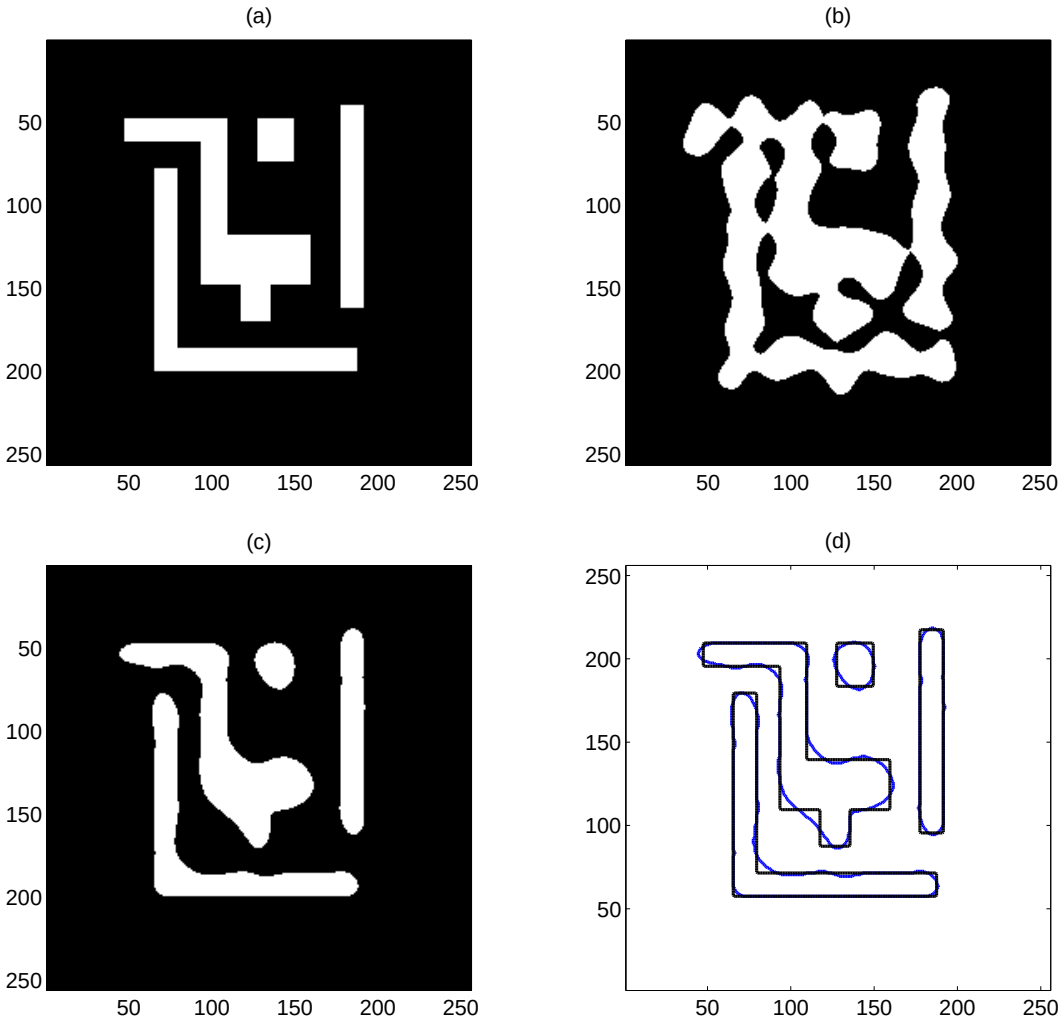

Figure 4.19: (a) Target mask, (b) outcome mask, (c) exposed region for 40%, (d) contour plot of target mask and the exposed region (exposed region is shown in dark blue color) for $N = 256$, $z = 0$, and 1.4% error.

We tested the accuracy of our results by using two different mask sizes, namely $N = 128$, and $N = 256$. Using higher resolution for mask increased our accuracy as expected. To compare with more realistic optical set up we also used finite values for z, and did not observe any significant change. We also tried mask with more complicated, smaller and narrowly spaced features. Even for these masks, our approach gave satisfactory results.

Chapter 5

Conclusions

In this thesis, we addressed one of the problems that arise in photolithography, that is the design of an optimum mask which can produce the desired pattern on a silicon wafer. Our goal was to formulate this as an inverse problem, and develop an algorithm that can be used to design such masks efficiently. After an introduction to scalar diffraction theory, and introducing our notation, we described the forward problem. One strong point of the SOCS approach was to write the aerial image intensity using singular value decomposition. This enabled us to calculate the eigenvalues and eigenfunctions once, and use the same values for different mask patterns. Note that these eigenvalues and eigenfunctions only depend on the optical parameters of the system.

We then formulated the inverse problem by defining a cost function. By using the calculus of variations, we showed that minimizing the cost function is equivalent to solving a level set equation. Our numerical results compared well with the existing literature, and we were able to successfully obtain mask designs that produced exposed patterns very close to the initially chosen complicated target patterns. Compared to traditional OPC in mask design, where corrections are done locally and sometimes by trial and error, this approach is more efficient, and is able to capture interactions caused by nearby features.

There are many other variables in mask design that may affect the outcome of a fabricated pattern. For instance optical aberrations may play a role, something we have ignored in our current study. In the future, we would like to incorporate such

lens aberrations in the intensity calculations and study their affect on the optimum mask design. In addition, the ability to capture sharp corners effectively still presents a challenge. Even though our algorithm produced better results compared to earlier work, we believe the results could even further be improved by choosing a more appropriate cost function.

We also would like to test these algorithms in close collaboration with experimentalists in nanofabrication. The masks obtained as an outcome of our numerical approach can be manufactured, and tested on real substrates, and final outputs can be compared. Similarly, more complicated designs that experimentalists are not able to manufacture on a wafer at a desired accuracy, can be tested with our model, without the actual cost of mask fabrication or etching.

Bibliography

[1] F. Schellenberg. "A Little Light Magic". *IEEE Spectrum* **40**, 34 (2003).

[2] N. B. Cobb. *Fast Optical and Process Proximity Correction Algorithms for Integrated Circuit Manufacturing.* PhD thesis, University of California at Berkeley, 1998.

[3] J. A. Sethian. Fast Marching Methods and Level Set Methods for Propagating Interfaces. In Van Kareman Institute, editor, *Computational Fluid Mechanics.* Von Karman Institute Lecture Series, 1998.

[4] L. F. Thompson, C. G. Wilson, and M. J. Bowden, editors. *Introduction to Microlithography.* ACS Professional Reference Book, 1994.

[5] J. W. Goodman. *Speckle Phenomena in Optics.* Roberts and Company, 2006.

[6] http://public.itrs.net. International Technology Roadmap for Semiconductors, 2007.

[7] N. B. Cobb and A. Zakhor. "Fast, Low-Complexity Mask Design". *Optical Microlithography, Proc. SPIE* **2440**, 313 (1995).

[8] A. Poonawala and P. Milanfar. "A Pixel-Based Regularization Approach to Inverse Lithography". *Microelectron. Eng.* **84**(12) (2007).

[9] S. Sayegh, B. Saleh, and K. Nashold. "Image Design: Generation of a Prescribed Image Through a Diffraction Limited System with High-contrast Recording". *IEEE Tran. on Acoustics, Speech and Signal Proc.* page 460 (1985).

[10] K. Nashold and B. Saleh. "Image Construction Through Diffraction-limited High Contrast Imaging System: An Iterative Approach". *J. Opt. Soc. Am. A* **2**, 635 (1985).

[11] S. Sherif, B. Saleh, and R. Leone. "Binary Image Synthesis Using Mixed Linear Integer Programming". *IEEE Tran. on Image Proc.* **4**, 1252 (1995).

[12] Y. C. Pati and T. Kailath. "Phase-shifting Masks for Microlithography: Automated Design and Mask Requirements". *J. Opt. Soc. Am. A* **11**(9) (1994).

[13] Y. Liu and A. Zakhor. "Binary and Phase Shifting Mask Design for Optical Lithography". *IEEE Tran. on Semicond. Manu.* **5**, 138 (1992).

[14] Y. Pati et.al. "An Error Measure for Dose Correction in E-beam Nanolithograhy". *J. Vacc. Sci. and Tech. B* **8**, 1882 (1990).

[15] M. C. Peckerar, S. Chang, and C. R. K. Marrian. "Proximity Correction Algorithms and a Co-processor Based on Regularized Optimization. Part I Description of The Algorithm". *J. Vacc. Sci. and Tech. B* **13**(2518-2525) (1995).

[16] M. C. Peckerar and C. R. K. Marrian. "Error Measure Comparison of Currently Employed Dose-Modulation Schemes for E-beam Proximity Effect Control". *Proc. SPIE* **2437**, 222 (1995).

[17] Y. Granik. "Solving Inverse Problems of Optical Microlithography". *Optical Microlithography, Proc. SPIE* **5754**, 506 (2005).

[18] R. D. Guenther. *Modern Optics*. John Wiley and Sons, 1990.

[19] G. R. Fowles. *Introduction to Modern Optics*. Holt, Rhinehart and Winston, Inc., 1975.

[20] J. W. Goodman. *Introduction to Fourier Optics*. Roberts and Company, 2005.

[21] W. C. Elmore and M. A. Heald. *Physics of Waves*. Dover, 1985.

[22] M. Born and E. Wolf. *Principles of Optics*. Pergamon Press, 1975.

[23] O. K. Ersoy. *Diffraction, Fourier Optics and Imaging*. John Wiley and Sons, 2007.

[24] H. H. Hopkins. "On the Diffraction Theory of Optical Images". *Proc. Royal Soc. London Ser. A* **217**, 408 (1953).

[25] H. Gamo. *Matrix Treatment of Partial Coherence*, volume 3 of *Progress in Optics*, chapter 3, pages 187–326. North-Holland Publishing Company, 1964.

[26] B. E. A. Saleh and M. Rabbani. "Simulation of Partially Coherent Imagery in the Space and Frequency Domains by Modal Expansion". *Applied Optics* **21**(15), 2770 (1982).

[27] H. Kirchauer. *Photolithography Simulation*. PhD thesis, Technical University of Vienna, Austria, 1998.

[28] H. H. Hopkins. "The Concept of Partial Coherence in Optics". *Proc. Royal Soc. London* (1951).

[29] R. A. Horn and C. R. Johnson. *Matrix Analysis*. Cambridge University Press, 1985.

[30] J. H. Wilkinson. *The Algebraic Eigenvalue Problem*. Oxford University Press, 1988.

[31] Y. C. Pati, A. A. Ghazanfarian, and R. F. Pease. "Exploiting Structure in Fast Aerial Image Computation for Integrated Circuit Patterns". *IEEE Tran. on Semicond. Manu.* **10**(1), 62 (1997).

[32] S. Osher and J. A. Sethian. "Fronts Propagating with Curvature Dependent Speed: Algorithms Based on Hamilton-Jacobi Formulations". *J. Comp. Phys.* **79**, 12 (1988).

[33] J. A. Sethian. "A Marching Level Set Method for Monotonically Advancing Fronts". *Proc. Nat. Acad. Sci.* **93**(4), 1591 (1996).

[34] J. A. Sethian. "Curvature and the Evolution of Fronts". *Comm. Math. Phys.* **101**, 487 (1985).

[35] F. Santosa. "A Level-set Aprroach for the Inverse Problems Involving Obstacles". *ESAIM Control Optim. Calc. Var.* **1**, 17 (1996).

[36] S. Osher and F. Santosa. "Level Set Methods for Optimizing Problems Involving Geometry and Constraints I. Frequencies of Two-Density Inhomogeneous Drum". *J. Comp. Phys.* **171**, 272 (2001).

[37] S. Osher and R. Fedkiw. *Level Set Methods and Dynamic Implicit Surfaces*. Number 153. Springer, 2000.

[38] D. Peng et. al. "A PDE-Based Fast Local Level Set Method". *J. Comp. Phys.* **155**, 410 (1999).

[39] D. L. Chopp. Recent Advance in the Level Set Method. In *Handbook of Biomedical Image Analysis*, volume 1, pages 201–254. Kluwer Academic, 2005.

[40] J. A. Sethian. "Numerical Algorithms for Propagating Interfaces: Hamilton-Jacobi Equations and Conservation Laws". *J. Differ. Geom.* **31**, 131 (1990).

[41] J. A. Sethian. *Level Set Methods: Evolving Interfaces in Geometry, Fluid Mechanics, Computer Vision, and Material Science*. Cambridge University Press, 1996.

[42] M. G. Crandall and P-L. Lions. "Viscosity Solutions of Hamilton-Jacobi Equations". *Tran. AMS* **277**, 1 (1983).

[43] M. G. Crandall, L. C. Evans, and P-L. Lions. "Some Properties of Viscosity Solutions of Hamiltonian-Jacobi Equations". *Tran. AMS* **282**, 487 (1984).

[44] L. C. Evans. *Partial Differential Equations, Berkeley Mathematics Lecture Series*, volume 3A,3B. Center for Pure and Applied Mathematics, University of California, Berkeley, CA, 1994.

[45] R Kimmel and J. A. Sethian. "Computing Geodesic Paths on Manifolds". *Proc. Nat. Acad. Sci.* **95**, 8431 (1998).

[46] F. Riesz and B. Sz.-Nagy. *Functional Analysis*. Dover, 1990.

Appendix A

A.1 Solid angle

Solid angles are analogous to simple angles in two dimensions (see Figure A.1). In two dimensions, an angle can be measured in radians. A radian is the arc length of a unit circle subtended by an angle, θ, defined as

$$\theta = \frac{\text{arc length}}{\text{radius}} .$$

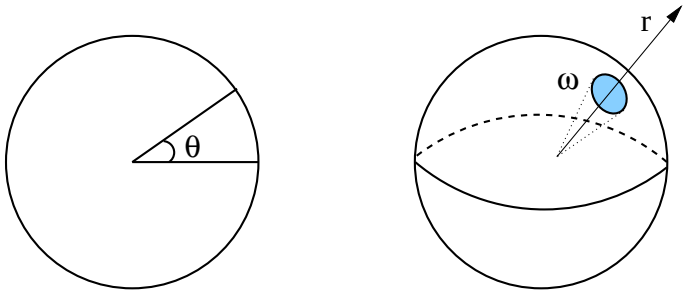

Figure A.1: The analogy between an angle and a solid angle

Similarly in three dimensions, a solid angle can be measured in *steradians*. A steradian is the surface area of a unit sphere subtended by the solid angle, ω. Hence one can

write

$$\omega = \frac{\text{surface area}}{\text{radius}^2}\,.$$

The surface area of a unit sphere has a steradian measure of 4π, whereas the circumference of a unit circle has a radian measure of 2π.

The differential area element and the solid angle are given by

$$\begin{aligned} dA &= (r\,d\theta)(r\,\sin\theta\,d\phi) = r^2\sin\theta\,d\theta\,d\phi \\ d\Omega &= \frac{dA}{r^2} = \sin\theta\,d\theta\,d\phi\,, \end{aligned}$$

respectively.

Appendix B

B.1 Hermitian Matrices and Quadratic Form.

The matrix (t_{ik}) of the transformation T is said to be *Hermitian symmetric* if $t_{ki} = t_{ik}^*$ or equivalently if we have

$$(Tx, x') = (x, Tx') \tag{B.1}$$

for all vectors x and x', there exist n characteristic vectors

$$e_i = (e_{i1}, e_{i2}, \ldots, e_{in}), \qquad (i = 1, 2, \ldots, n) \tag{B.2}$$

corresponding to the characteristic values μ_i and forming an orthonormal system. Let z_i denote the components of the vector x with respect to the new system of coordinates formed with respect to those vectors e_i as follows:

$$x = z_1 e_1 + z_2 e_2 + \ldots + z_n e_n \,. \tag{B.3}$$

Then *the quadratic (Hermitian) form*

$$(Tx, x) = \sum_{i,k=1}^{n} t_{ik} x_i^* x_k, \qquad (t_{ki} = t_{ik}^*) \tag{B.4}$$

transforms into purely quadratic form

$$\sum_{i=1}^{n} \mu_i z_i^* z_i, = \sum_{i=1}^{n} \mu_i \left| z_i \right|^2 \ . \tag{B.5}$$

This is the so called *theorem of principal axes* from algebra [46].

B.2 Composite Trapezoidal Rule

Consider the integral

$$A = \int_a^b f(x)\, dx. \tag{B.6}$$

Suppose that the interval $[a, b]$ is divided into N subintervals $[x_i, x_{i+1}]$ of width $\Delta x = (b-a)/N$ by using equally spaced nodes $x_i = a + (i-1)\,\Delta x$, for $i = 1,\, 2, \ldots,\, (N+1)$. The trapezoidal rule—which approximates the area under one strip by the area of a trapezoid—can then be expressed as

$$A \approx \frac{\Delta x}{2} \sum_{i=1}^{N} f(x_i) + f(x_{i+1}) = \frac{\Delta x}{2}(f(x_1) + f(x_{N+1})) + \Delta x \sum_{i=2}^{N} f(x_i)\,. \tag{B.7}$$

In two dimensions, the double integral

$$S = \int_a^b \int_c^d f(x, y)\, dx\, dy\,, \tag{B.8}$$

extended to a rectangle $x = a,\ x = b,\ y = c,\ y = d$, can be evaluated numerically by applying two successive integrations, using the trapezoidal rule for single integration shown in Eq. (B.7), in the x and y directions. Assume that this rectangle is divided into equally spaced, $N \times M$ rectangles with sides $\Delta x = (b-a)/N$ and $\Delta y = (d-c)/M$. Then by applying the trapezoidal rule twice, one in x direction and another in y direction, we

obtain,

$$\begin{aligned} S &\approx \frac{\Delta x\,\Delta y}{4}\left[f(x_1,y_1)+f(x_{N+1},y_1)+f(x_1,y_{M+1})+f(x_{N+1},y_{M+1})\right] \\ &+ \frac{\Delta x\,\Delta y}{2}\left[\sum_{i=2}^{N}\left(f(x_i,y_1)+f(x_i,y_{M+1})\right)+\sum_{j=2}^{M}\left(f(x_1,y_j)+f(x_{N+1},y_j)\right)\right] \\ &+ \Delta x\,\Delta y\sum_{i=2}^{N}\sum_{j=2}^{M} f(x_i,y_j)\,, \end{aligned} \tag{B.9}$$

where $x_i = a + (i-1)\,\Delta x$, for $i = 1, 2, \ldots, (N+1)$ and $y_j = c + (j-1)\,\Delta y$, for $j = 1, 2, \ldots, (M+1)$. By introducing weighting coefficients $w_{i,j}$ one can write Eq. (B.9) as

$$S \approx \frac{\Delta x\,\Delta y}{4}\sum_{i=1}^{N+1}\sum_{j=1}^{M+1} w_{i,j}\, f(x_i,y_j) \tag{B.10}$$

where the weighting coefficients are chosen as

$$\begin{aligned} w_{i,j} &= 1 \text{ for } (i,j) = (1,1),\ (1,M+1),\ (N+1,1),\ (N+1,M+1) \\ &= 4 \text{ for } i = 2,3,\ldots,N \text{ and } j = 2,3,\ldots,M \\ &= 2 \text{ for other } i \text{ and } j \text{ combinations.} \end{aligned} \tag{B.11}$$